catalysts

MDPI

Review

Recent Advances of Oxygen Carriers for Hydrogen Production via Chemical Looping Water-Splitting

Wenxi Chang [1,2], Yue Hu [2,3], Weibin Xu [2,3], Chuande Huang [2,*], Haonan Chen [1], Jiahui He [1], Yujia Han [2,3], Yanyan Zhu [1,*], Xiaoxun Ma [1] and Xiaodong Wang [2,*]

[1] School of Chemical Engineering, Northwest University, International Scientific and Technological Cooperation Base of MOST for Clean Utilization of Hydrocarbon Resources, Chemical Engineering Research Center for the Ministry of Education for Advance Use Technology of Shanbei Energy, Xi'an 710069, China
[2] CAS Key Laboratory of Science and Technology on Applied Catalysis, Dalian Institute of Chemical Physics, Chinese Academy of Sciences, Dalian 116023, China
[3] School of Chemical Engineering, University of Chinese Academy of Sciences, Beijing 100049, China
* Correspondence: huangchuande@dicp.ac.cn (C.H.); zhuyanyan@nwu.edu.cn (Y.Z.); xdwang@dicp.ac.cn (X.W.)

Abstract: Hydrogen is an important green energy source and chemical raw material for various industrial processes. At present, the major technique of hydrogen production is steam methane reforming (SMR), which suffers from high energy penalties and enormous CO_2 emissions. As an alternative, chemical looping water-splitting (CLWS) technology represents an energy-efficient and environmentally friendly method for hydrogen production. The key to CLWS lies in the selection of suitable oxygen carriers (OCs) that hold outstanding sintering resistance, structural reversibility, and capability to release lattice oxygen and deoxygenate the steam for hydrogen generation. Described herein are the recent advances in designing OCs, including simple metal oxides (e.g., Fe, Zn, Ce, and Ti-based metal oxides) and composite metal oxides (e.g., perovskite, spinel, and garnets), for different CLWS processes with emphasis on the crucial parameters that determine their redox performance and future challenges.

Keywords: chemical looping; water-splitting; hydrogen; oxygen carrier; redox performance

Citation: Chang, W.; Hu, Y.; Xu, W.; Huang, C.; Chen, H.; He, J.; Han, Y.; Zhu, Y.; Ma, X.; Wang, X. Recent Advances of Oxygen Carriers for Hydrogen Production via Chemical Looping Water-Splitting. *Catalysts* **2023**, *13*, 279. https://doi.org/10.3390/catal13020279

Academic Editor: Edward G. Gillan

Received: 20 December 2022
Revised: 12 January 2023
Accepted: 19 January 2023
Published: 26 January 2023

1. Introduction

An urgent desire to reduce reliance on fossil fuels has been spurred in recent years due to the steeply increased concentration of greenhouse gases in the atmosphere [1]. Hydrogen, as an alternative, has been regarded as a promising fuel that possesses a high calorific value (121.00 MJ/kg) that is 2.8 times and four times greater than petroleum and coal, respectively, while giving clean water as the only combustion product [2–4]. More importantly, hydrogen is an important chemical raw material for various industrial processes, such as crude oil refining, synthesis of ammonia and methanol, etc. [5]. Currently, the production of hydrogen is mainly based on fossil fuels, such as steam methane reforming (SMR) and coal gasification (CG) [2,6,7]. However, both commercial routes are energy-intensive, rendering massive CO_2 emissions reaching as high as 10–16 and 22–35 $kgCO_2e/kgH_2$ for the SMR and CG processes, respectively [8–11]. Although carbon capture and storage technologies can potentially reduce the CO_2 emissions, this would inevitably induce a significant increase in energy penalty and manufacturing costs [12,13].

As a reverse reaction of hydrogen combustion, hydrogen production directly from water-splitting is considered a sustainable approach. Intuitively, direct thermal splitting of water ($H_2O(l) \rightarrow H_2(g) + 1/2O_2(g)$, ΔH^0_{298} = 286 kJ/mol) is the simplest method to implement this goal. However, thermodynamic analysis shows that a positive Gibbs free energy is maintained for this reaction until a temperature higher than 4370 K (Figure 1), revealing an extremely tough process to break the O–H bond in H_2O molecules [14].

Kogan et al. [15] proposed that water conversion only reached ca. 25% at a temperature of 2500 K and pressure of 0.05 bar, and rapid cooling treatment was needed to suppress the reverse reaction between generated H_2 and O_2, causing an increased energy burden. A study showed that hydrogen produced by pyrolyzing the mixture of water and argon was lower than 3% percentage of all off-gases at 2000~2500 °C [16]. Recent reports suggested that water-splitting driven by light and electricity enabled production of hydrogen at ambient temperature [17,18]. Compared with the photocatalytic process that is still in its infancy, electrochemical water-splitting could provide roughly 5% of the world's hydrogen energy [19]. The purity of hydrogen generated in the electrolysis process is high, but the electrolysis process consumes a large amount of power, and the electricity cost accounts for around 80% of the overall water electrolysis process, rendering the scale-up of this technology strongly depending on the availability of low-cost and green electricity [20–22]. Therefore, research is ongoing to explore more efficient methods for hydrogen production with low carbon emissions and energy penalty.

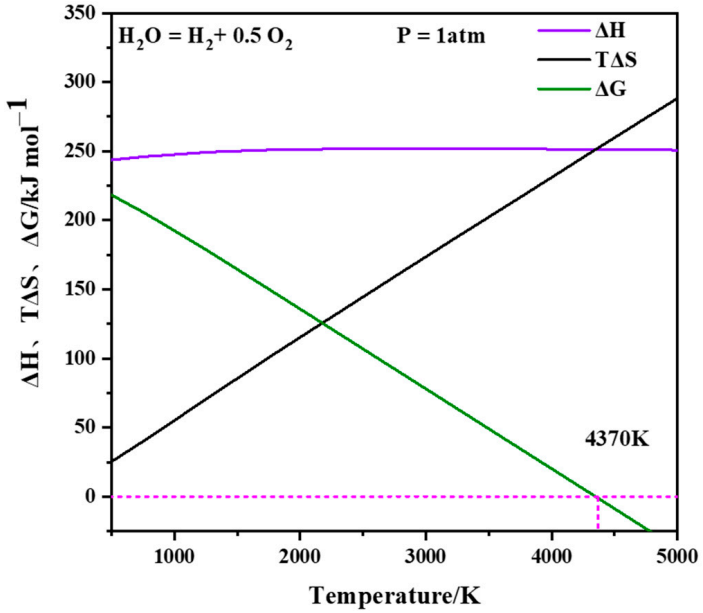

Figure 1. Variation of ΔH, TΔS, and ΔG with the temperature for direct water-splitting at 1 atm. Adapted with permission from Ref. [14], copyright 2007, American Chemical Society.

Chemical looping technology that was initially designed as an advanced combustion method has shown great potential for energy storage and production of chemicals due to the virtue of process intensification, leading to improved process efficiency and notably reduced CO_2 emission and investment expenses [23–25]. In recent years, pioneering reports have verified that applying the chemical looping concept to water-splitting, known as chemical looping water-splitting (CLWS), enables efficient hydrogen production at temperatures below 1300 °C. Compared with continuous reaction mode, CLWS reaction, utilizing metal oxides as oxygen carriers (OCs), is fulfilled by two or three spatiotemporal separated steps, including abstracting lattice oxygen from OCs via reduction treatment, regeneration by water with production of hydrogen, and in some cases, further oxidation by air to fully recover the OCs. Such a multistep reaction not only affords great convenience in separating hydrogen from products, but also requires less useful work and reaction free energy changes for water decomposition [26,27]. Furthermore, the introduction of OCs as redox catalysts significantly lowers the threshold to break the O–H bond of H_2O and improves the reaction kinetics [28–30].

In general, the yield of hydrogen in a single redox cycle is positively correlated with the oxygen capacity of OCs, which in turn is closely related to the reduction method to remove the lattice oxygen. According to the distinct strategies in abstracting lattice oxygen

from OCs, CLWS can be classified into processes including a two-step thermochemical water-splitting cycle (thermal reduction, Figure 2A) [31], a methane chemical looping process (CH_4 reduction, Figure 2B), a chemical looping water gas shift reaction (CO reduction, Figure 2C) [32], a syngas (mixture of H_2 and CO) chemical looping process (syngas reduction, Figure 2D) [33], and a photo-thermochemical cycle (photochemical reduction, Figure 2E) [34]. As for CLWS reaction, the economic efficiency of hydrogen production is substantially determined by redox properties of OCs, including mechanical strength, oxygen capacity, reactivity, selectivity, and structural stability, as well as low toxicity and low cost [35,36]. A series of reviews have been proposed in recent years that comprehensively summarized the potential applications of chemical looping technology [37], reaction mechanism of OCs [38], and the recent advantages in OCs for chemical looping conversion of alkanes [39–41]. As for hydrogen production via the chemical looping method, Voitic et al. [42] have reviewed the progress with emphasis on the iron-based OCs, while Luo et al. [43] detailed the system integration, economic analysis, and OCs for the chemical looping reforming process (cofeeding the fuel and water to reactor) and fuel-driven chemical looping water-splitting. Herein, the review gives a detailed survey on the current state of OC development for hydrogen production via different CLWS processes. The effect of the inherent properties of OCs on feed-gas conversion or product selectivity and future challenges in designing the OCs are summarized.

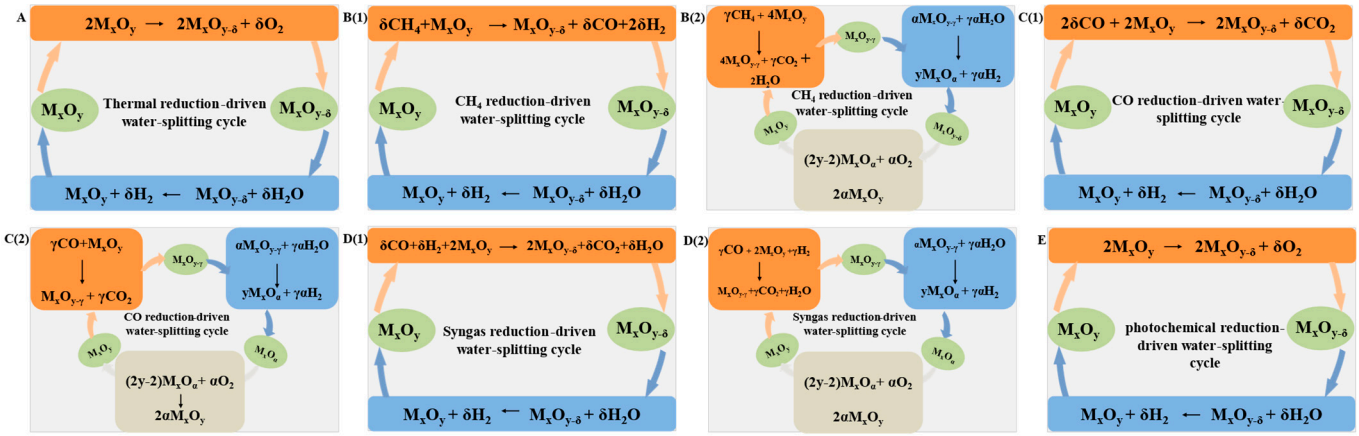

Figure 2. Chemical looping water-splitting process with various reducing methods: (**A**) two-step water-splitting thermochemical cycle, (**B**) methane chemical looping process, (**C**) chemical looping water gas shift process, (**D**) syngas chemical looping process, and (**E**) photo-thermochemical cycle.

2. Processes for Chemical Looping Water-Splitting

2.1. Two-Step Thermochemical Water-Splitting

To address the problems of high reaction temperature and low conversion for direct water-splitting, in 1966 Funk et al. [26] proposed the strategy of two-step thermochemical water-splitting (TCWS) for hydrogen production. The key to this process lies in selecting suitable metal oxides as OCs, which are thermally reduced at high temperature (>1300 °C) to release oxygen and subsequently recovered by H_2O at a temperature generally lower than 1100 °C with production of hydrogen. As a result, direct contact between hydrogen and oxygen is avoided, which bypasses the issue of hydrogen separation and enables higher water conversion at lower temperatures. In particular, when concentrated solar energy is utilized to heat the OCs (two-step solar thermochemical cycles), the solar energy is transformed to chemical energy with a theoretical solar-to-fuel efficiency reaching higher than 70% [14]. However, the high reaction temperature and thermal shocks induced by temperature swing pose a huge challenge in designing the OCs [44,45].

The Fe_3O_4/FeO redox pair was one of the earliest OCs used in a two-step TCWS cycle. Based on the thermodynamic analyses, Nakamura et al. [46] and Steinfeld et al. [47] reported that it was feasible to apply Fe_3O_4/FeO for hydrogen generation via thermochemical cycle

at temperatures of ca. 2000 °C (Figure 3). However, these oxides were subjected to severe sintering under high operating temperatures. To address this issue, some active metals or inert supports were introduced to the OCs in an attempt to lower the thermal reduction temperature or improve their sintering resistance. Han et al. [48] found that removal of lattice oxygen from ferrites was realized at lower temperature of 1200 °C after doping of Ni, Mn, and Cu while water-splitting was implemented at 800 °C. Among the screened materials, $NiFe_2O_4$ displayed the highest rate for hydrogen production with an average H_2 yield of 0.442 mL/g (the amount of produced H_2 per gram of oxygen carrier in each cycle). Structural analysis revealed that no obvious changes occurred after these redox reactions, which demonstrated a high stability of this material. Kodama et al. [49,50] also suggested that Ni-modified ferrites in $A_xFe_{3-x}O_4$ (A = Mn, Co, Ni) exhibited better reactivity than Co or Mn promoters, and a scaling relationship between Ni content (from 0 to 1) with corresponding performance was noticed. When Ni loading increased to x = 1, a maximum hydrogen productivity of ca. 10 mL/g is reached. Their follow-up studies showed that loading of ferrites on ZrO_2 support significantly slowed down the sintering process, leading to stable hydrogen production. Ishihara et al. [51] reported that combination of $NiFe_2O_4$ with YSZ (yttrium-stabilized zirconia) support was capable of promoting the redox stability and oxygen mobility, resulting in a negligible decline in hydrogen production in 10 continuous cycles with reduction temperature of 1773 K and water-splitting temperature of 1473 K. Miller et al. [52] proposed that a mass ratio of 1/3 for $Co_{0.67}Fe_{2.33}O_4$/YSZ could effectively inhibit the agglomeration of OCs and enable stable hydrogen production during eight cycles. In contrast, the bare $Co_{0.67}Fe_{2.33}O_4$ oxides was inactivated in the second cycle.

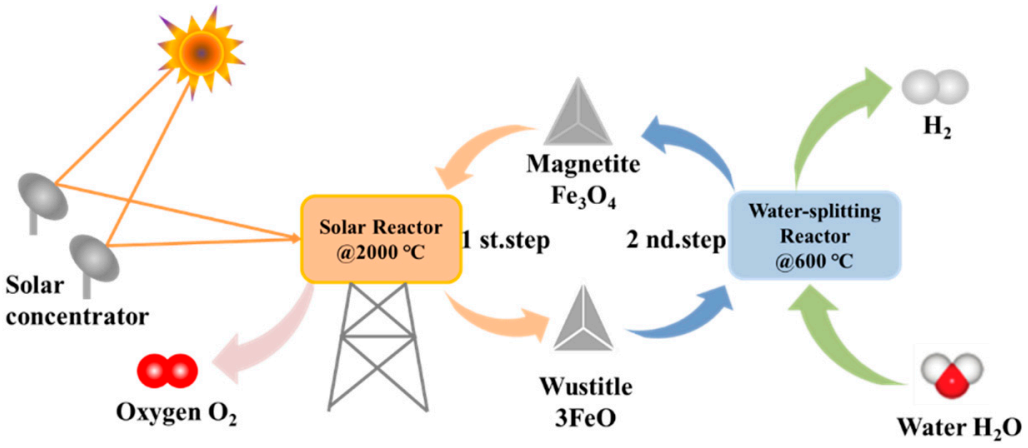

Figure 3. Schematic for two-step solar thermochemical water-splitting using Fe_3O_4/FeO redox system. Adapted with permission from Ref. [47], Copyright 1999, Elsevier.

In 1977, Bilgen's team [16] applied a ZnO/Zn redox pair to the two-step TCWS cycle. Experimental results proved that thermal decomposition of ZnO into gaseous Zn (boiling point of 907 °C) and O_2 was achieved at 2338 K using a solar furnace. Thermodynamic calculations showed that the theoretical solar-to-fuel efficiency (without heat recovery) of the water-splitting cycle could reach 51% when the redox cycle was conducted with thermal reduction temperature of 2338 K (ZnO decomposition) and water-splitting at 1500 K. However, practical application of ZnO in TCWS remains greatly challenging due to the facile recombination of Zn and O_2 before introduction of water; thus, a quench treatment is necessary to separate Zn from O_2 by rapid condensation of Zn gas into solid form. The numerical simulation results by Palumbo et al. [53] showed that a conversion of 80% was achieved for ZnO decomposition when a high solar flux density of 2 MW/m^2 and quenching rate of 2.0 × 10^7 K/s were applied. Another challenge for application of ZnO/Zn redox pairs lies in the formation of a ZnO shell during the water-splitting reaction ($Zn + H_2O \rightarrow ZnO + H_2$), which significantly slows down the reaction kinetics [54].

Therefore, recent works have been devoted to kinetic study on this process with the aim to improve the hydrogen production efficiency. Ernst et al. [55] investigated the reaction between submicron zinc and ~50 mol% H_2O/Ar at 603–633 K. It was found that the initial reaction was a surface-controlled process with a fast rate and apparent activation energy of 42.8 ± 7.4 kJ/mol, while the subsequent reaction was a slow diffusion control process due to the restriction of surface ZnO layer on the migration of Zn^{2+}. Lv et al. [56] investigated the effect of particle size on the water-splitting process and found that zinc powder with different sizes exhibited similar hydrolysis mechanisms, but that reducing the particle size could significantly enhance the reaction rate.

CeO_2, as a benchmark OC for two-step TCWS, has attracted particular attention since 2006 due to its outstanding redox properties. Abanades et al. [57] found that Ce_2O_3 obtained by thermal reduction of CeO_2 can be facilely oxidized by water with a conversion reaching 100%. However, a temperature of above 2000 °C is needed for complete reduction of CeO_2 to Ce_2O_3, which inevitably resulted in serious sintering of OCs. To bypass this issue, in most cases for TCWS applications, the reduction temperature was lowered to below 2000 °C, leading to formation of non-stoichiometric $CeO_{2-\delta}$. Steinfeld et al. [58] reported that 2.5~2.9 mL of O_2 can be released per gram of ceria in a single redox cycle (2.5~2.9 mL/g), corresponding to δ value of 0.039~0.044, when thermal reduction was conducted at ca. 1600 °C. This rendered a hydrogen evolution rate reaching a peak value of 7.6×10^2 mL/min during the following water-splitting step (<900 °C), which resulted in an overall solar-to-hydrogen efficiency of 0.7%. Costa Oliveira et al. [59] investigated the effect of CeO_2 morphology on water-splitting reaction and discovered that H_2 yield over three-dimensionally ordered macroporous (3DOM) CeO_2 was approximately 32% greater than that of conventional CeO_2 foam, suggesting that engineering the morphology was effective in adjusting the reaction kinetics and oxygen mobility. Although much progress has been achieved these years, the low oxygen capacity and high reduction temperature of pure ceria greatly limited the hydrogen productivity and process efficiency, which impeded the feasibility of ceria in practical STWS applications. To address this issue, significant research has been performed to tailor the redox properties of Ce-based OCs by tuning the oxygen vacancies and lattice strain via doping foreign cations [60–63]. Gokon et al. [64] compared the performance of 30 mol% M-doped CeO_2 (M = Fe, Co, Ni, or Mn) in two-step TCWS cycles and found that all dopants except for Ni greatly increased the oxygen evolution during thermal reduction at 1500 °C. However, the yield of H_2 is lower than that of bare CeO_2, which may be ascribed to severe sintering of these OCs at high temperature. Tamaura et al. [65] investigated the performance of CeO_2-MO_x solid solution (M = Mn, Fe, Ni, Cu) with Ce/M molar ratio of 9 for two-step TCWS. As shown in Figure 4A, introducing of di- or tri-valent transition metal cations into CeO_2 notably promoted H_2 generation by enhancing releasing of lattice oxygen. The same group further screened a series of $Ce_{0.9}M_{0.1}O_{2-\delta}$ ceramics (M = Mg, Ca, Sr, Sc, Y, Dy, Zr, and Hf), and found that the evolution of O_2 (reduction of Ce^{4+} to Ce^{3+}) in the thermal reduction step was improved by doping cations with higher valence state and smaller effective ionic radius (Figure 4B) [66,67]. Furthermore, the amount of H_2 produced in the water-splitting step was dominated by the amount of O_2 released in the reduction step. Instead, Abanades and coworkers [68] showed that addition of tri-valent dopants, including Y, La, Pr, and Gd, mainly contributed to improve the sintering resistance rather than the reducibility of ceria, but the ceria/zirconia mixed oxide was capable of greatly enhancing the reduction of bulk Ce^{4+}. After detailed study on the correlation between zirconium content and redox properties of $Ce_{1-\delta}Zr_\delta O_2$ ($0 \leq \delta \leq 0.5$), it was found that the ratio of Ce^{3+}/Ce^{4+} in thermally reduced oxides gradually increased with Zr content while an optimal composition of $Ce_{0.75}Zr_{0.25}O_2$ gave the highest hydrogen yield of 6.67 mL/g [69,70]. Their follow-up studies suggested that decoration of CeO_2-ZrO_2 with 1% Gd results in further promotion of hydrogen production to 7.58 mL/g [71]. Instead of exploring the nonstoichiometric chemistry that results in partial reduction of Ce^{4+} to Ce^{3+}, Wang et al. [72] discovered that Sn-modified oxide of CeO_2-xSnO_2 (x = 0.05–0.20) was converted to thermodynami-

cally stable $Ce_2Sn_2O_7$ during the thermal reduction step (1400 °C), which enabled deep reduction of Ce^{4+} to Ce^{3+} rather than $CeO_{2-\delta}$. When the Sn content was optimized to x = 0.15, a hydrogen production as high as 7.18 mL/g (Figure 5), 3.8 times greater than that of unmodified CeO_2, was obtained.

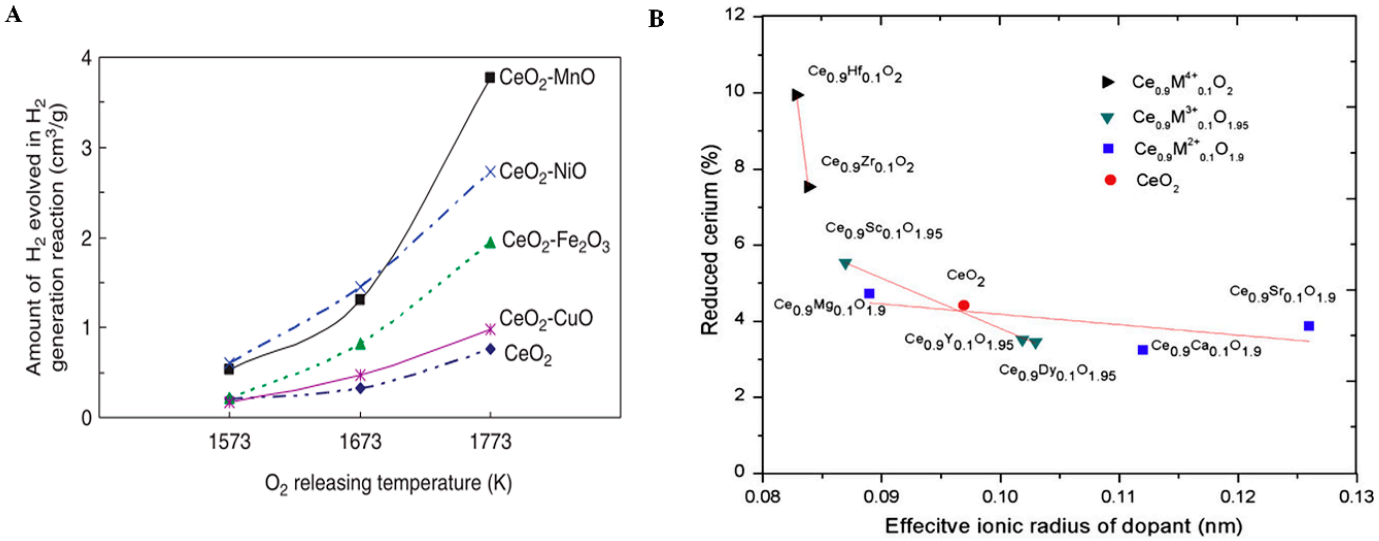

Figure 4. (**A**) Correlation between O_2-releasing temperature and the amount of hydrogen produced in the reaction with CeO_2–MO_x. Reprinted with permission from Ref. [65], copyright 2007, Elsevier. (**B**) Effect of effective ionic radius and valence state of dopants on the reduction degree of cerium. Reprinted with permission from Ref. [66], copyright 2011, Elsevier.

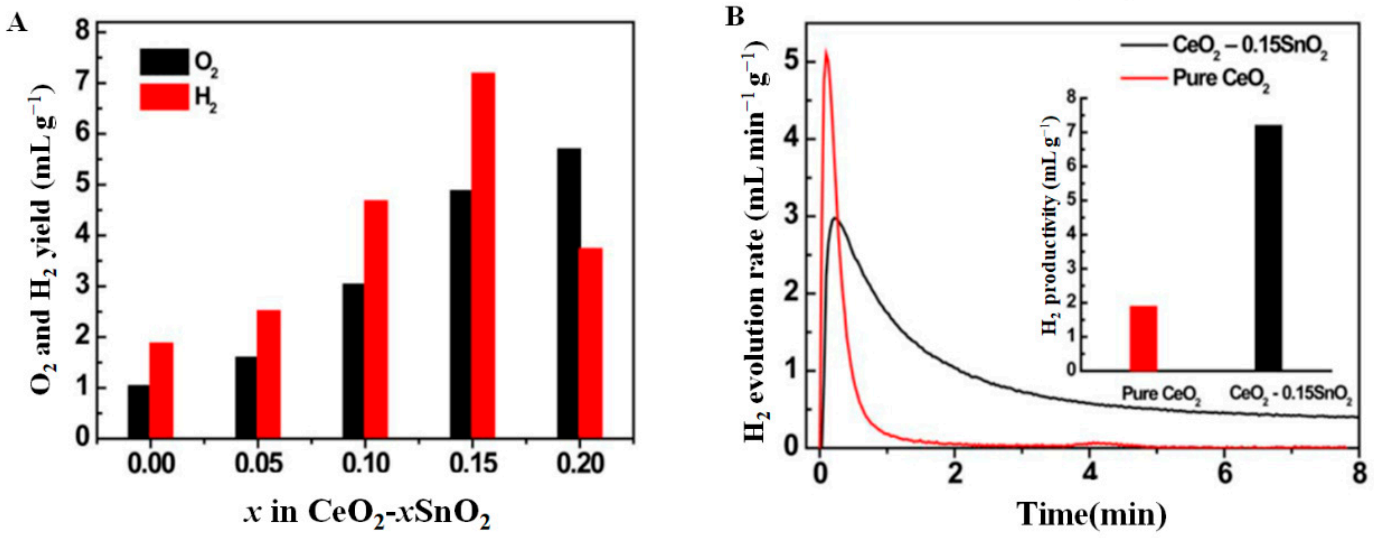

Figure 5. (**A**) Evolution of O_2 and H_2 for $CeO_{2-x}SnO_2$ (x = 0.05–0.20) during redox reactions. (**B**) H_2 evolution rate during water-splitting reaction at 800 °C for CeO_2–0.15SnO_2 and pure CeO_2. Adapted with permission from Ref. [72], Copyright 2017, Wiley.

Perovskite oxides (ABO_3) represent an important class of composite materials, wherein the A-site is generally occupied by rare earth, alkaline earth, or alkali metals that coordinate with 12 oxygen anions while the B-site is typically occupied by transition metals located in the octahedral interstices of the oxygen framework. These oxides hold virtue of outstanding redox properties, structure reversibility, and high-temperature stability, which render these oxides promising OCs for two-step TCWS reactions [73,74]. McDaniel et al. [75] discovered that Sr/Al doped $LaMnO_3$ exhibited exceptional oxygen mobility, which released 8 times more O_2 than CeO_2 at 1350 °C, while the temperature for lattice oxygen

desorption was nearly 300 °C lower than that of CeO_2. Consequently, a hydrogen yield 9 times greater than that of CeO_2 is obtained at 1000 °C. R. Barcellos and colleagues [76] demonstrated that doping of Ce at B-site of $BaMnO_{3-\delta}$ allowed optimization of the oxygen vacancy formation energy. Among the investigated $BaCe_xMn_{1-x}O_{3-\delta}$ samples ($0 \leq x \leq 1$), $BaCe_{0.25}Mn_{0.75}O_{3-\delta}$ displayed the best water-splitting performance and yielded nearly 3 times more hydrogen than ceria when reduced at 1350 °C. Similarly, Li et al. [31] also found that introduction of Co into $LaGaO_3$ notably reduced the oxygen vacancy formation energy to ca. 3.0 eV, which was favorable for both lattice oxygen desorption and subsequent water-splitting. The best $LaGa_{0.4}Co_{0.6}O_{3-\delta}$ sample exhibited a H_2 yield of 0.478 mmol/g that was 15 times greater than CeO_2 (0.032 mmol/g) when reduced at 1350 °C and re-oxidized at 800 °C. Carter et al. [77] screened a series of $Ca_{0.5}Ce_{0.5}MO_3$ oxides (M = Sc, Ti, V, Cr, Mn, Fe, Co, and Ni) for a two-step solar thermochemical process using density functional theory (DFT) calculations. The calculation results suggested that the oxygen vacancy formation energy of $Ca_{0.5}Ce_{0.5}MnO_3$ and $Ca_{0.5}Ce_{0.5}FeO_3$ was slightly lower than that of CeO_2 (4.0~4.3 eV) and located in the range of 3.65~3.96 and 3.77~4.06 eV, respectively, which fitted well to the target window (3.2~4.1 eV) for thermochemical cycles (Figure 6). Qian et al. [78] found that the $CaTi_{0.5}Mn_{0.5}O_{3-\delta}$ was favorable for oxygen releasing and water-splitting due to its intermediate reduction enthalpy value of 200–280 KJ/mol-O (the standard enthalpy to remove one mole lattice oxygen of OC) and large entropy value of 120–180 J/mol-O·K (the standard entropy to remove one mole lattice oxygen of OC), which enables a hydrogen production of 10.0 mL/g in redox cycle between 1350 °C (thermal reduction) and 1150 °C (water-splitting) with a short cycle time of 1.5 h. All these results indicate that perovskite oxides are among the best candidates for two-step TCWS processes, and that A/B site engineering is efficient in modulating their redox properties. However, the step forward for practical application of this technology is still greatly hindered by high operating temperature and relatively low hydrogen yield due to the low oxygen redox capacity and long temperature swing time, which should be resolved ultimately by developing more effective OCs.

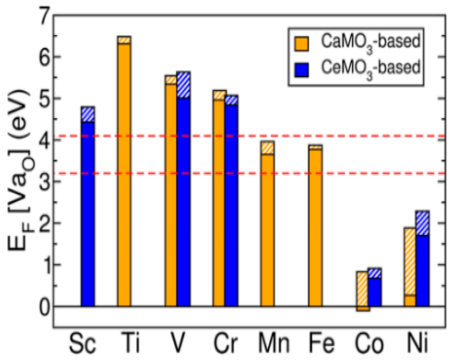

Figure 6. Oxygen vacancy formation energy of $Ca_{0.5}Ce_{0.5}MO_3$ perovskites derived from $CaMO_3$ (orange bars) and $CeMO_3$ (blue bars) oxides. Red dashed lines show the target scope for solar thermochemical hydrogen production (3.2~4.1 eV). Reprinted with permission from Ref. [77], copyright 2020, American Chemical Society.

2.2. Methane Chemical Looping Process

The two-step TCWS cycle approach has substantially decreased the reaction temperature (≤1500 °C) compared to direct thermal splitting of water, but the high reaction temperature still puts forward tough requirements for the reaction equipment. Furthermore, the continuous temperature swing and thermal shock during the cyclic reaction not only reduces the reaction efficiency but also leads to rapid decrease of redox performance, which seriously limits the commercialization of this technology. To this end, recent reports verified that introduction of reducing gas could significantly accelerate the reduction kinetics of OCs, lower the reaction temperature to below 1000 °C, and increase the amount of lattice oxygen desorption, substantially enhancing the hydrogen production efficiency [79–83].

Methane, the main component of natural gas, has been widely studied due to its abundant reserves, high hydrogen-to-carbon ratio, and strong reducibility [84,85]. The two-step TCWS cycle with methane as reducing gas is commonly referred to as methane chemical looping process (Figure 2B). The facile reduction of OCs in methane atmosphere enables a closed reaction loop at much milder conditions, which potentially reduces the energy penalty and improves the economics of this process. Compared with conventional standalone systems that generate hydrogen and electricity separately based on methane, it is assessed that chemical looping hydrogen generation with methane as reduction gas was able to save more than 16% of energy input while reducing beyond 98% of CO_2 emissions, rendering a low cost of $32.87/MWh for H_2 production [86].

The methane conversion over OCs undergoes different processes, including partial oxidation or total combustion, when modulating the redox properties of these oxides. As for OCs with relatively low reducibility, syngas production is favored by selective methane oxidation ($CH_4 + O_L \rightarrow CO + 2\ H_2$) (Figure 2B1). The reduced OCs can be subsequently recovered by water oxidation with generation of hydrogen ($H_2O \rightarrow O_L + H_2$). The overall reaction is generally referred as chemical looping steam methane reforming (CL-SMR) [87]. Compared with traditional steam methane reforming reaction ($CH_4 + H_2O \rightarrow CO + 3\ H_2$), the CL-SMR process can obtain syngas with H_2/CO ratio of 2, which is suitable for Fischer–Tropsch synthesis and methanol. Furthermore, pure hydrogen is produced separately from syngas, bypassing the gas separation process; more importantly, through the rapid cycling of these OCs in different reactors, coking deposition on the catalyst is greatly inhibited [88–91]. When OCs with high reducibility are applied, methane is fully oxidized to CO_2 and H_2O ($CH_4 + 4\ O_L \rightarrow CO_2 + 2\ H_2O$), which is a strong exothermic reaction, and the released heat can be used for the next step water-splitting reaction, achieving heat self-sufficiency. Another dramatic difference between such a process with CL-SMR is that a third step by air oxidation is normally required to fully regenerate the OCs due to their high oxidation potential (Figure 2B2). This process (three reactors chemical looping M-TRCL) enables hydrogen production with low CO_2 emissions, since the high concentration of CO_2 can be captured by simple condensation [92].

2.2.1. Supported or Doped Iron Oxides

As for methane-driven three step CLWS, the studied OCs are mainly focused on iron oxides, which holds the virtue of low cost and environmentally friendly features [93,94]. However, developing an efficient method to avoid coke formation, which can degrade the hydrogen purity in the water-splitting step, over these OCs during methane atmosphere remains a great challenge [95]. Ku et al. [96] reported that methane dissociation and coke formation occurred over Fe_2O_3/Al_2O_3 OCs due to the generation of the $FeAl_2O_4$ phase, since the newly formed phase displayed poor oxygen mobility and rendered notably decreased oxygen capacity of OC for chemical looping reactions. To address this issue, Xiang et al. [97] proposed that loading Fe_2O_3 to $MgAl_2O_4$ support greatly suppressed the solid-phase reaction between iron oxides and the support, thereby restraining the carbon formation from CH_4 dissociation. Furthermore, they found that K-promoted Fe_2O_3/Al_2O_3 further improved the resistance towards coke deposition by decreasing the reduction activity of oxygen carrier. Li et al. [98] found that a combination of mixed ionic-electronic conductive (MIEC) support of $La_{0.8}Sr_{0.2}FeO_3$ with Fe_2O_3 improved lattice oxygen diffusion from the bulk to surface, which promoted the elimination of carbon during the methane reduction process.

Instead, when syngas is set as aimed products (methane-driven two-step CLWS), the proper OC needs to bear sufficient reactivity for selective methane conversion. There is usually a seesaw effect in reactivity and selectivity due to the proportional relationship between C–H bond activation ability of CH_4 and oxidation ability [99]. For instance, common iron oxides (Fe_2O_3 and Fe_3O_4) are reactive towards methane conversion, but CO_2 production is preferred over these OCs due to the high oxygen capacity [100,101]. To improve the selectivity of syngas at the CL-SMR process, extensive efforts have been

made to break the seesaw effect. Fan et al. [102] proposed that decreasing the particle size of Fe_2O_3 to 3–5 nm by confining these oxides in mesoporous SBA-15 (Fe_2O_3@SBA-15) enabled notable enhanced syngas selectivity to above 99%. Corresponding DFT calculations demonstrated that the low coordinated Fe and O atoms of Fe_2O_3 nanoparticles promoted CH_4 activation, cleavage of Fe–O bond, and formation of CO while suppressed the further oxidation to CO_2 (Figure 7). Based on DFT + U calculations, they further analyzed the mechanism for CH_4 partial oxidation over α-Fe_2O_3 and claimed that increasing the oxygen vacancy concentration decreased the activation barriers for breaking the C–H bonds of CH_4 and Fe–C bonds, which contributed to improved reactivity and syngas selectivity (Figure 8) [103]. Recently, Wang's team [104] discovered that Y-modified Fe_2O_3/Al_2O_3 (Y: Fe = 1.5) could produce a new phase of $Y_3Fe_2Al_3O_{12}$ garnet after high temperature treatment (1200 °C), which increased the dispersion of active metal Fe, and changed the coordination environment of oxygen species. Lattice oxygen could coordinate with Fe, and also coordinate with Al and Y (Fe-O-Al, Fe-O-Y), which renders increased oxygen vacancy formation energy from 1.4 eV for bear Fe_2O_3 to 1.997 eV of $Y_3Fe_2Al_3O_{12}$, which substantially avoids excessive oxidation of CH_4 to CO_2 while maintaining CO selectivity as high as 98%.

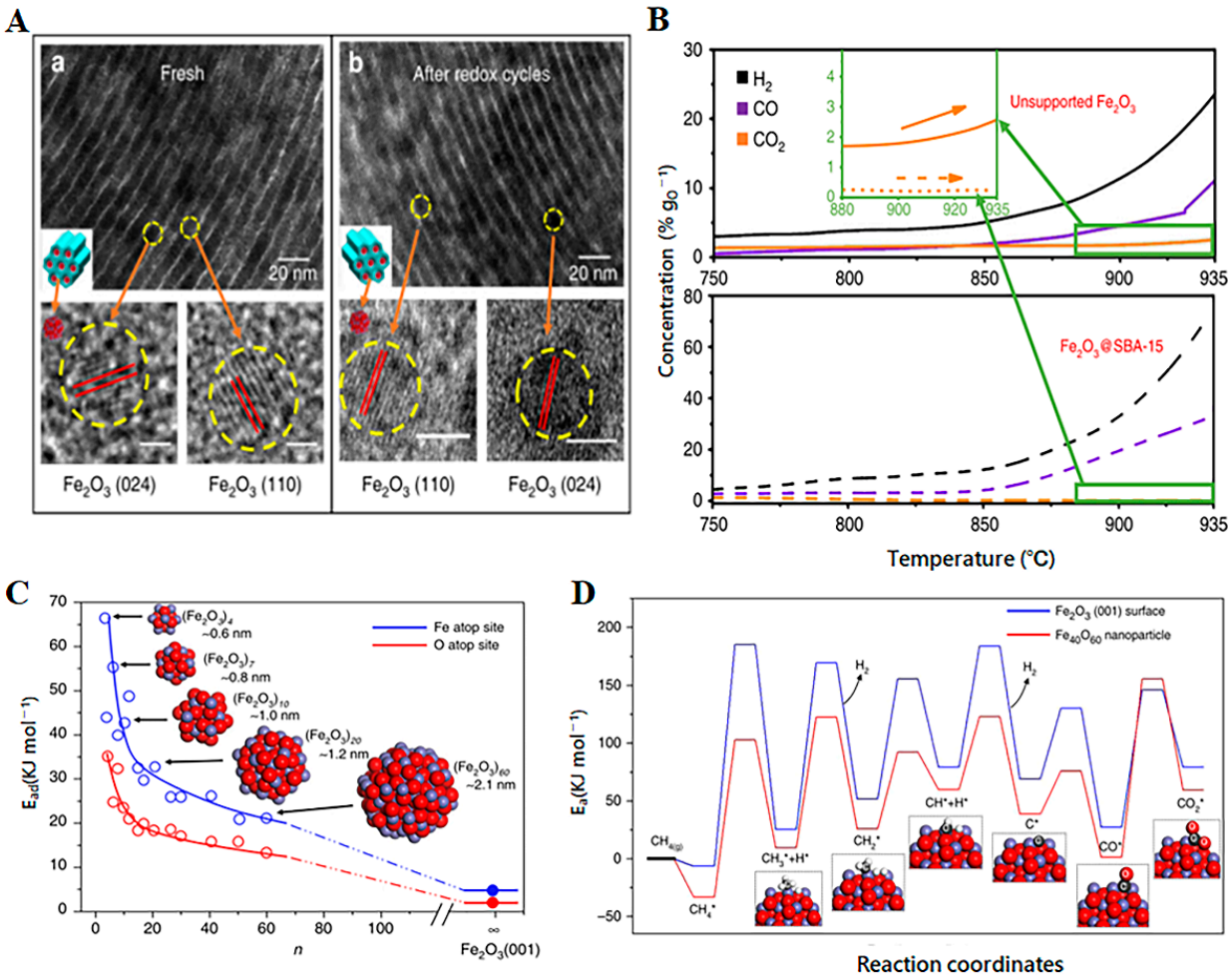

Figure 7. (**A**) Morphological characteristics of Fe_2O_3@SBA-15 OC. (**Aa**) HR–TEM images of fresh Fe_2O_3@SBA-15 and typical Fe_2O_3 nanoparticles (scale bar of 1 nm); (**Ab**) HR–TEM images of Fe_2O_3@SBA-15 after 75 cycles and typical Fe_2O_3 nanoparticles (scale bar of 5 nm); (**B**) Temperature programmed reduction profiles of Fe_2O_3@SBA-15 and unsupported Fe_2O_3; (**C**) Calculated results of CH_4 adsorption on Fe atop site and O atop site of $(Fe_2O_3)_n$ nanoparticles; (**D**) Energy evolution of CH_4 conversion on $Fe_{40}O_{60}$ nanoparticle and Fe_2O_3 (001) surface. Adapted with permission from Ref. [102], copyright 2019, Nature.

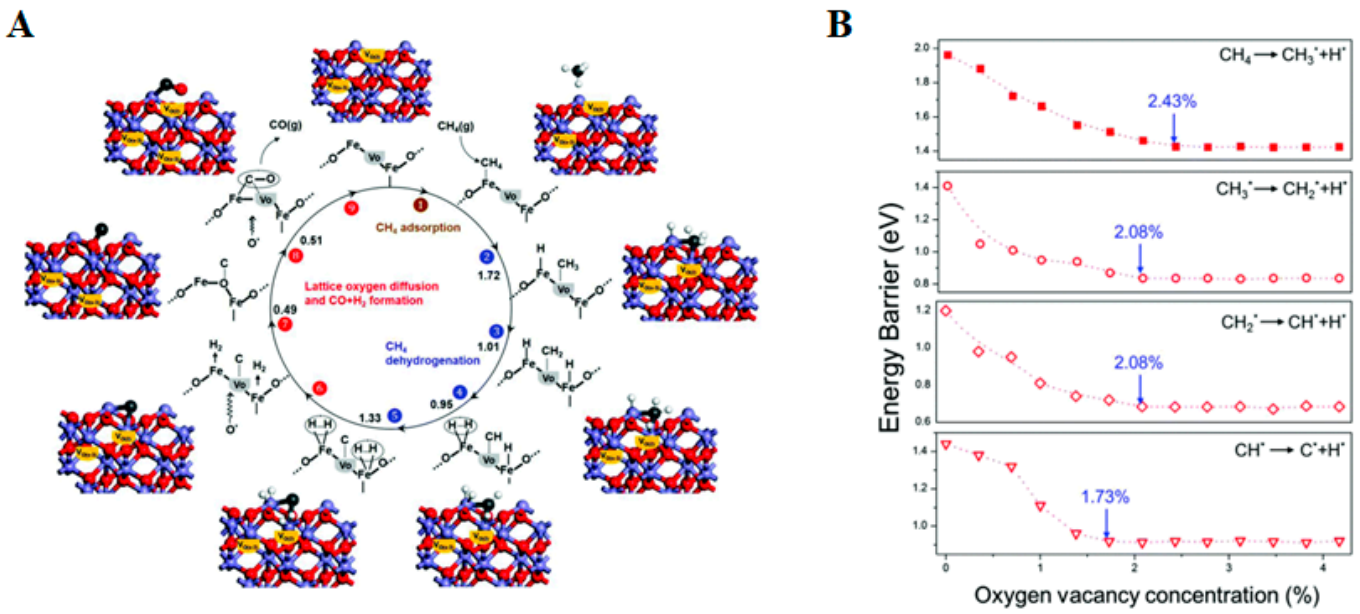

Figure 8. (**A**) Mechanism for CH_4 partial oxidation over α-Fe_2O_3 (001) surface with oxygen vacancies. Inset of the reaction loop is the activation barrier (eV) for each elementary step. V_O represents the surface oxygen vacancy. (**B**) The correlation between activation energy of C–H bond and the oxygen vacancy concentration of α-Fe_2O_3 (001) surface. Reprinted with permission from Ref. [103], copyright 2016, Royal Society of Chemistry.

2.2.2. Supported or Doped Cerium Oxides

Cerium-based OCs have been widely studied for CL-SMR in terms of their high oxygen storage capacity and reliable resistance to carbon deposition [105–107]. However, pure CeO_2 exhibits low reactivity towards methane conversion and is prone to sintering in several cyclic reactions. Therefore, great effort has been applied to improve the reactivity and stability of these OCs by doping foreign cations and constructing composite oxides. Wang et al. [108] discovered that Ni-modified (5 wt%) CeO_2-TiO_2 enabled 100% conversion of CH_4, ca. 16 times greater than that of pure CeO_2-TiO_2 (5.9%), with 85% syngas selectivity at 900 °C. A mechanism study showed that Ni species accounted for the main active centers for CH_4 activation and promoted the reduction of Ce^{4+} (CeO_2-TiO_2) to Ce^{3+} ($Ce_2Ti_2O_7$) (Figure 9B). The synergy between active Ni species and CeO_2-TiO_2/$Ce_2Ti_2O_7$ redox oxides significantly increased the water-splitting performance with hydrogen yield up to 47.0 mL/g (Figure 9). Zhu et al. [87,109,110] prepared a series of Fe-doped cerium oxides ($Ce_{1-x}Fe_xO_{2-\delta}$) for a CL-SMR process and discovered that introduction of iron notably improved the reducibility of OCs, and formation of Ce-Fe-O solid solution ($CeFeO_3$) could enhance the lattice oxygen migration, leading to increased methane conversion. As for the optimized sample (x = 0.5), conversion of methane approached 60% with syngas selectivity exceeding 80% and hydrogen productivity of 83.3 mL/g. Li et al. [111] loaded Ce-Fe-Zr-O oxides (40 wt%) onto inert MgAl-LDO (magnesium–aluminum layered double oxides) and demonstrated that the redox reactivity and stability were greatly improved due to the highly dispersed active components, accelerated reaction between Ce-Fe oxides, and restrained sintering of OCs. Experimental results showed that methane conversion decreased from 58% to 46% in the first 6 cycles and stayed steady in the following 14 cycles with CO selectivity maintained over 80% and hydrogen yield of 1.0 mmol/g. This group further studied the synergy between CeO_2 and 3DOM-$LaFeO_3$ during CL-SMR reactions and found that 10 wt% CeO_2/$LaFeO_3$ displayed the highest yields of syngas (9.94 mmol/g) and hydrogen (3.38 mmol/g), since the interaction of CeO_2-$LaFeO_3$ generated a great number of oxygen vacancies that promoted lattice oxygen diffusion and restricted the carbon deposition [112]. Zhu et al. [113] also found an obvious synergetic effect between CeO_2 and $BaFe_3Al_9O_{19}$ (BF3). The difference was that a new phase of $CeFe_xAl_{1-x}O_3$ was generated

during chemical looping reactions, which resulted in promoted diffusion of lattice oxygen and increased methane conversion to ca. 90%. Wei et al. [114] investigated the influence of OCs morphology on the redox reactivity and found that CeO_2/ZrO_2 oxides calcined at low temperatures (450 °C) held stable 3DOM structure with uniform particle size, which effectively enhanced the migration of oxygen species and improved the reactivity for CH_4 partial oxidation and water-splitting. After 10 cycles at 800 °C, a hydrogen yield exceeding 38.89 mL/g was maintained.

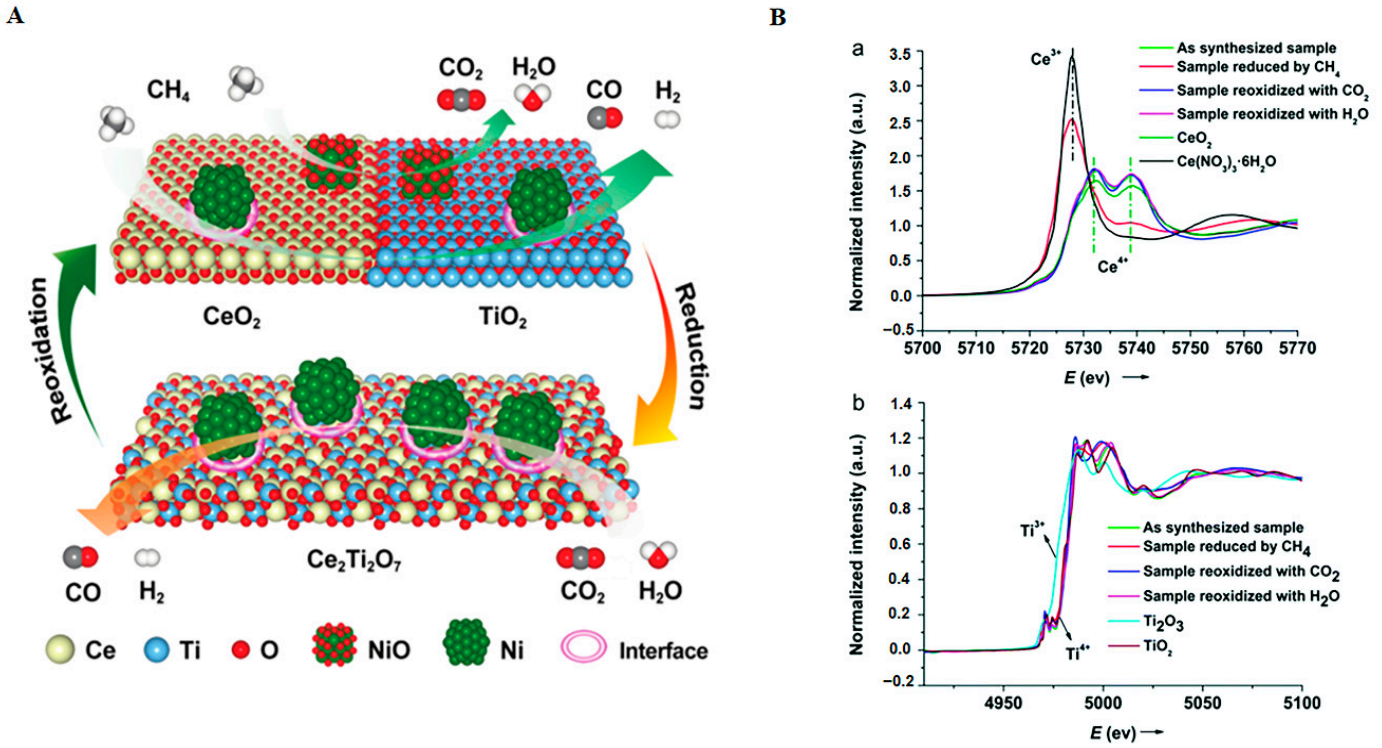

Figure 9. (**A**) Proposed mechanism for MDR–STCDS and MDR–STWS processes over $5Ni/CeO_2–TiO_2$. (**B**) Normalized XANES profiles for $5Ni/CeO_2–TiO_2$ after various steps during isothermal MDR–STCDS and MDR–STWS reactions at (**Ba**) the Ce L_{III}–edge and (**Bb**) the Ti K-edge, together with the spectra of reference compounds. Adapted with permission from Ref. [108], copyright 2019, Royal Society of Chemistry.

2.2.3. Perovskites

Perovskite oxides are promising OCs for CL-SMR due to their excellent redox activity [115,116]. Lee et al. [117] discovered that doping Fe in B-site of $LaCoO_3$ improved lattice oxygen mobility, reactivity for partial oxidation of CH_4, and adsorption and dissociation of H_2O, which enabled high CO selectivity of 92% and H_2 purity of 99.3% during the methane reduction and water-splitting steps, respectively. Gong and colleagues [118,119] discovered that substitution of Ce^{3+} for La^{3+} of $LaFeO_3$ was capable of tuning lattice oxygen activity via modulating the distortion degree of FeO_6 octahedra. When Ce/La ratio reached 1 ($La_{0.5}Ce_{0.5}FeO_3$), the oxygen carrier had the lowest oxygen vacancy formation energy and the highest oxygen mobility, which rendered the best methane-to-syngas and water-splitting performance. Furthermore, the yield of hydrogen (0.6 mmol/g) remained stable during 100 redox cycles (Figure 10), highlighting the outstanding stability of this OC. Recently, Wang et al. [120] proposed that the reactivity of lattice oxygen in $LaFe_{0.8}M_{0.2}O_3$ (M = Al, Fe, Ga, Sc) perovskite was not only influenced by B-site cations, but also greatly affected by the La cations at A-site. It was found that a decline of FeO_6 tilting degree by doping smaller cations at B-site of $LaFe_{0.8}M_{0.2}O_3$ was beneficial to weaken the La–O interaction, thereby improving the mobility of lattice oxygen and methane conversion performance. The researchers [121] further showed that doping Sr and Al at A and B sites

of $LaFeO_3$, respectively, significantly promoted the deep reduction of $Fe^{4+/3+}$ cations to Fe^0 by forming Fe^0@oxides intermediate with core-shell structure. Moreover, the core-shell structure formed in methane atmosphere was able to prevent direct contact between CH_4 and Fe^0, which promoted syngas production and suppressed coke deposition over Fe^0 (Figure 11). Li's group [122] discovered that doping of Fe in $LaMnO_3$ greatly enhanced the redox performance due to lattice distortion and increased concentration of oxygen vacancy. Among the screened oxides, $La_{0.85}MnFe_{0.15}O_3$ displayed the highest CO selectivity of ~99% and hydrogen yield of 1.76 mmol/g. Similar results could be observed for Ni or Co modified $LaMnO_3$ [123]. Li et al. [124] designed an OCs of Fe_2O_3@$La_xSr_{1-x}FeO_3$ (LSF) with core-shell structure and found that LSF not only improved the diffusion of lattice oxygen in Fe_2O_3 but also reduced the direct contact between CH_4 and Fe_2O_3, which resulted in highly selective CH_4-to-syngas conversion with selectivity as high as 89%. Zhao et al. [125] found that $LaFe_{1-x}Co_xO_3$ (x = 0, 0.2, 0.4, 0.6, 0.8) with a 3DOM structure promoted the mass transfer and provided more active centers for CH_4 conversion. Moreover, Co doping increased oxygen mobility, which reduced carbon deposition and improved the purity of hydrogen. This group [126] further investigated the synergistic effect of different metals in double perovskite $La_{1.6}Sr_{0.4}FeCoO_6$, and found that CH_4 was prone to be activated on cations with high valence state (Fe^{5+}, Fe^{4+}, and Co^{3+}), while the correspondingly formed Fe^{2+}, Co^0 and the oxygen vacancies provided rich active centers for splitting of H_2O.

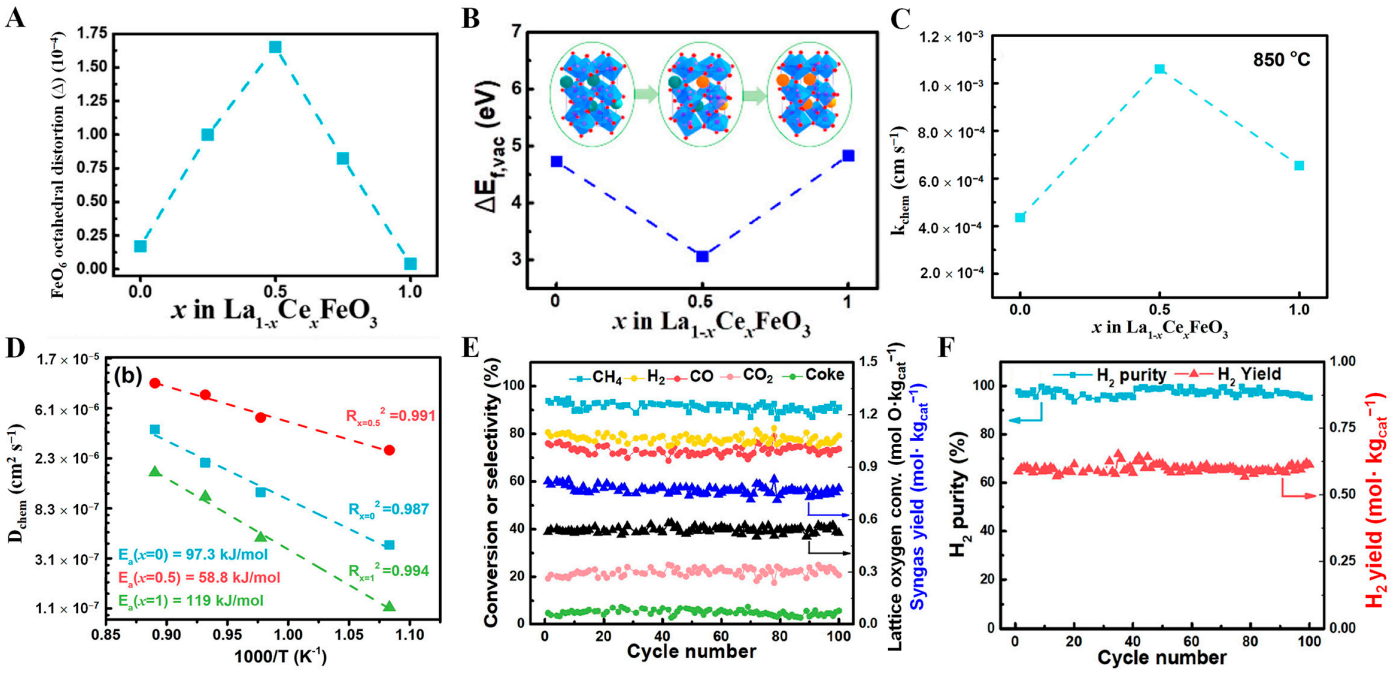

Figure 10. (**A**) Distortion degree (Δ) of FeO_6 octahedra for $La_{1-x}Ce_xFeO_3$ (x = 0, 0.25 0.5, 0.75, 1) and (**B**) calculated oxygen vacancy formation energy ($\Delta E_{f,vac}$) of $La_{1-x}Ce_xFeO_3$ (x = 0, 0.5, 1). Adapted with permission from Ref. [119], copyright 2020, American Chemical Society. (**C**) The oxygen surface exchange coefficient (k_{chem}) and (**D**) bulk diffusion coefficient (D_{chem}) of $La_{1-x}Ce_xFeO_3$ (x = 0, 0.5, 1). Redox performance of (**E**) CH_4 partial oxidation step and (**F**) the H_2O-splitting step over $La_5Ce_5FeO_3$ in CL–SRM at 925 °C. Adapted with permission from Ref. [118], copyright 2020, Elsevier.

2.3. Chemical Looping Water Gas Shift Process

As a low-cost but important platform chemical, CO can be used as a reductant-like methane to drive the CLWS process and produce high-value hydrogen (Figure 2C) [127,128]. Herein, OCs were reduced by CO ($CO + O_L \rightarrow CO_2$) and subsequently regenerated by water ($H_2O \rightarrow O_L + H_2$). This process is generally known as a chemical looping water gas shift (CL-WGS) reaction due to the same overall reaction as that of water–gas shift reaction ($CO + H_2O \rightarrow CO_2 + H_2$). Compared with CL-SMR, the application of CO as a

reducing atmosphere can avoid the carbon deposition caused by CH_4 decomposition while the coke formation from the Boudouard reaction ($2CO \rightarrow C + CO_2$) is thermodynamically constrained at a temperature above 800 °C, which inhibited the contamination of hydrogen by carbon monoxide ($C + H_2O \rightarrow CO + H_2$). Furthermore, the separation of CO/CO_2 from H_2O/H_2 in chemical looping reactions also prevents the reverse water–gas shift reaction ($CO_2 + H_2 \rightarrow CO + H_2O$), leading to increased efficiency for water-splitting. Thermodynamic analysis demonstrated that the steam conversion in CL-WGS reaction reached 95% at 800 °C, which is significantly higher than the traditional WGS process [32]. Based on the ASPEN Plus simulation calculation, Zeng et al. [129] found that the thermal efficiency of H_2 production by a chemical looping process, including reduction of OCs by coal and CO (reducer reactor), partial oxidation of OC by steam oxidation to produce hydrogen (oxidizer reactor), and completely recovery of OC by air (combustor), could reach 78% for HHV (higher heating value) efficiency, which was much higher than that of hydrogen production from the traditional coal gasification method.

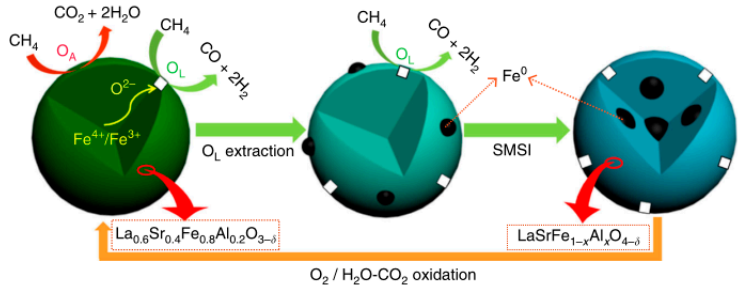

Figure 11. Proposed structural evolution of $La_{0.6}Sr_{0.4}Fe_{0.8}Al_{0.2}O_{3-\delta}$ OC during chemical looping partial oxidation of methane. White boxes represent the coordination unsaturated Fe cations. Reprinted with permission from Ref. [121], copyright 2018, Nature.

As for CL-WGS, the suitable OCs should be reactive for CO oxidation and subsequent water-splitting while possessing high redox stability. Fe_2O_3 has been widely studied due to the features of abundant reserves, favorable thermodynamic properties, and high oxygen-carrying capacity [130]. However, Fe_2O_3 is prone to agglomerate during several redox cycles, rendering rapid decline of hydrogen productivity. Recent works showed that loading of Fe_2O_3 on some inert supports, including ZrO_2 [131], Al_2O_3 [132,133], and $MgAl_2O_4$ [134], were effective in improving the specific surface area of OCs and slowing down the sintering process. Ma et al. [135] investigated in detail the effects of redox inert supports on the reactivity, redox stability, and hydrogen yield of Fe_2O_3/support OCs (support = Al_2O_3, SiO_2, $MgAl_2O_4$, and ZrO_2). It was found that the hydrogen yield of Fe_2O_3/Al_2O_3 and Fe_2O_3/SiO_2 gradually decreased with cyclic numbers, since solid phase reaction between Al_2O_3 or SiO_2 and Fe_2O_3 induced formation of less reactive $FeAl_2O_4$ and $FeSiO_3$, respectively. In contrast, when $MgAl_2O_4$ was utilized, the solid phase interaction between Fe_2O_3 and support was greatly inhibited, leading to improved redox stability and hydrogen yield of 54~93 mL/g. Yuzbasi et al. [136] reported that Na-modified Fe_2O_3/Al_2O_3 could generate a layered Na-β-Al_2O_3 phase to restrict the formation of $FeAl_2O_4$, which increased the redox stability and rendered a stable hydrogen production of 13.3 mmol/g during 15 cycles. Compared with these inert supports, introduction of MIEC support showed a much-pronounced effect in improving the efficiency of hydrogen production by enhancing migration of lattice oxygen and electron conductivity [137]. Ma et al. [138] studied the performance of $A_xCe_{1-x}O_{2-\delta}$ (A = Y, Sm and La) supported Fe_2O_3 for CL-WGS and found that Sm doping ($Fe_2O_3/Ce_{0.7}Sm_{0.2}O_{1.9}$) exhibited the best oxygen anion conductivity and oxygen mobility, which facilitated the conversion of CO and subsequent hydrogen production. In contrast, the reactivity of OCs was negatively correlated with La content due to the decreased oxygen capacity arising from formation of $LaFeO_3$ during the reaction. They further discovered that Zr and Sm co-doped $Fe_2O_3/Ce_{0.8}A_{0.2}O_{2-\delta}$ (A = Zr

and Sm) displayed better CO conversion and sintering resistance, rending a hydrogen yield of 54.25 mL/g for water-splitting [139].

Iron spinels that bear features of low cost, high thermal stability, and good oxygen mobility are promising OCs for chemical looping reactions [140,141]. Huang et al. [142] found that $NiFe_2O_4/Al_2O_3$ displayed stable H_2 yield during 20 cycles of CL-WGS, since Al_2O_3 support significantly inhibited the sintering of $NiFe_2O_4$. Kim et al. [143] also found that Al-modified $NiFe_2O_4$ exhibited good performance for water-splitting due to the formation of a spinel solid solution with Al, which could prevent densification of $NiFe_2O_4$. For the optimized sample with Al content of 3.3 wt%, maximum hydrogen productivity of 8.2 mmol/g was reached. Cui et al. [144] reported that the active Fe could completely exsolve from mixed Zn-Fe-Al spinel in CO atmosphere and resolved into spinel structure by water oxidation, enabling a hydrogen yield of 2.23 mmol/g with nearly 100% conversion of CO. More importantly, an embedded interface structure was formed for the reduced OC, which effectively limited Fe agglomeration and improved the reactivity and stability of the OCs. Based on DFT+U calculations, Xiao et al. [145] demonstrated that the reactivity of binary spinel AFe_2O_4 (A = Co, Cu, Ni, Mn) was mainly related to the concentration of oxygen vacancies (reduction level of OCs). Among these OCs, Co-modified OC was the best candidate for CL-WGS due to its suitable oxygen vacancy formation energy (2.70 eV) and lattice oxygen diffusion energy (1.03 eV), which gave an impressive yield of 11.9 mmol/g with average hydrogen production rate of 0.051 mmol/g·s at 650 °C (Figure 12). They further discovered that the oxygen vacancy formation energy and oxygen diffusion energy further decreased to 1.69 eV and 0.83 eV, respectively, after further doping of Cu in $CoFe_2O_4$ ($Cu_{0.25}Co_{0.25}Fe_{2.5}O_4$), which promoted the reduction kinetics in CO environment and increased the redox efficiency for hydrogen production. As a result, a hydrogen production as high as ~11.9 mmol/g was achieved at a temperature of 550 °C [146].

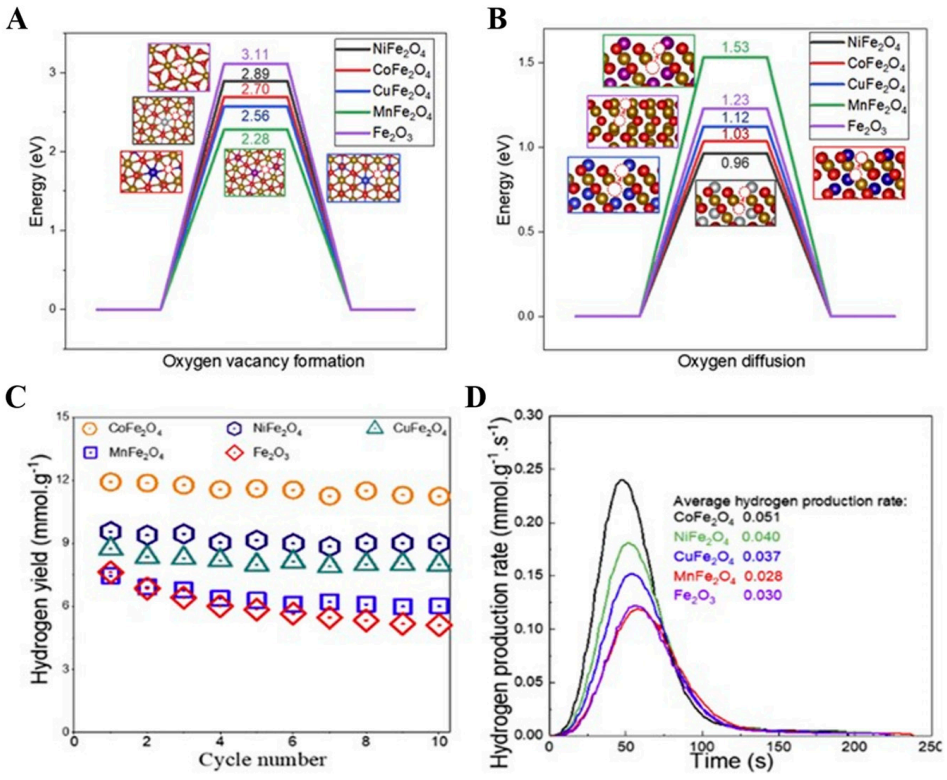

Figure 12. (**A**) The oxygen vacancy formation energy and (**B**) diffusion energy of lattice oxygen in $CoFe_2O_4$ (100), $CuFe_2O_4$ (100), $NiFe_2O_4$ (100), $MnFe_2O_4$ (100), and Fe_2O_3 (001) surfaces. O, Cu, Co, Ni, Mn, and Fe atoms are shown with red, light blue, dark blue, light grey, purple, golden spheres, respectively. (**C**) Profiles of the activation energy and (**D**) the hydrogen yield for different OCs. Reprinted with permission from Ref. [145], copyright 2019, Elsevier.

Brownmillerite ($Ca_2Fe_2O_5$) is well known for high oxygen capacity and excellent thermal stability due to the anion-deficient structure with alternating FeO_6 octahedral and FeO_4 tetrahedral layers [147,148]. Based on the thermodynamic study, Ismail et al. [149] found that the valence state of Fe in $Ca_2Fe_2O_5$ only displayed Fe^0 and Fe^{3+} without intermediate Fe^{2+} during the redox reactions, and Fe^0 could be directly oxidized to Fe^{3+} by steam, which was suitable for a water-splitting reaction. Chan et al. [150] discovered that the steam conversion over $Ca_2Fe_2O_5$ could reach 75%, which was much higher than that of Fe_2O_3/ZrO_2 (62%). Through thermogravimetric experiments, Sun et al. [151] found that $Ca_2Fe_2O_5$ displayed much faster reaction kinetics than $CaFe_2O_4$ during the CO reduction step, rendering a higher reduction degree of 94.0% (85.5% for $CaFe_2O_4$). Guo et al. [152] employed DFT calculations to explore the mechanisms of CO adsorption, oxidation, and oxygen anion diffusion on the surface of $Ca_2Fe_2O_5$ (010). It was discovered that CO preferred to adsorb on FeO_2- and FeO-terminated surfaces rather than CaO- and OCa-terminated surfaces, while the chemisorption energy of FeO_2-terminated surfaces was considerably greater than that of FeO-terminated surfaces. In addition, it is also proposed that the oxygen anion diffusion at high temperature was the rate-limiting step because the energy barrier of oxygen diffusion was significantly greater than that of the CO oxidation process (Figure 13).

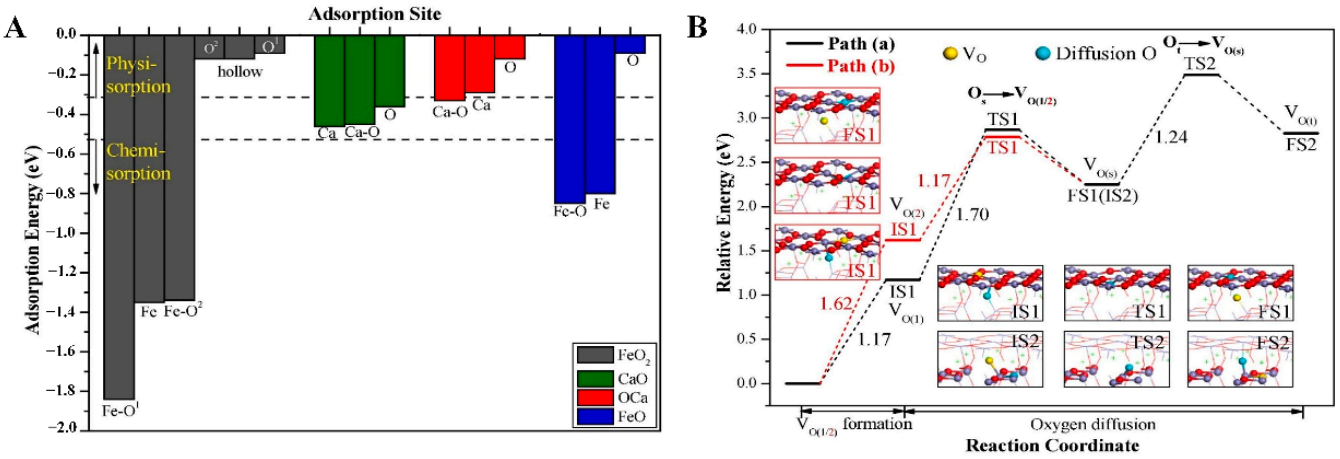

Figure 13. (**A**) Comparison of CO adsorption energies on FeO_2-, CaO-, FeO-, and OCa-terminated $Ca_2Fe_2O_5$ (0 1 0) surfaces. (**B**) The pathways and energy profiles for oxygen diffusion in $Ca_2Fe_2O_5$. Adapted with permission from Ref. [152], copyright 2020, Elsevier.

2.4. Syngas Chemical Looping Process

Syngas that can be produced via various routes, e.g., gasification of biomass, coal, and methane reforming, and represents another promising reducing agent for CLWS [153–155]. In the syngas-promoted CLWS process (Figure 2D), referred to as syngas chemical looping (SCL), syngas was utilized as the reducing gas instead of CO, while subsequent water-splitting and air oxidation (in some cases) were needed to recover the OCs. The focused OCs explored for this process are mainly iron-based oxides.

Fan et al. [33] investigated the feasibility of Ni, Cu, Cd, Co, Mn, Sn, and Fe oxides for SCL through thermodynamic analysis, and found that Fe_2O_3 exhibited the best syngas and steam conversion. The Fe_2O_3 OC displayed stable redox performance during 10 cycles at 600 °C and possessed a low attrition rate of 0.57% during the redox process in entrained flow reactor [156]. When a moving bed reactor was utilized, they found that a syngas conversion of 99.95% with Fe_2O_3 conversion close to 50% was achieved at 900 °C [157]. Dou et al. [158] showed that the syngas generated by in situ decomposition of glycerol was effective for reduction of OCs. Among the investigated OCs with different Ce/Ni/Fe molar ratios (0/0/1; 10/1/100, 10/3/100, 5/1/100, 5/2/100), OC with Ce/Ni/Fe ratio of 10/3/100 displayed the highest H_2 yield of 11.79 mmol/g at 750 °C. Mechanism stud-

ies suggested that Ni dopants promoted glycerol conversion while Ce could effectively improve the dispersion of Ni, the sintering resistance, and lattice oxygen mobility, thus substantially boosting the hydrogen yield. Sun et al. [159] investigated the performance of CeO_2-modified Fe_2O_3/Al_2O_3 in SCL process and found that CeO_2 could coordinate with Fe to generate more oxygen vacancies, which promoted the participation of lattice oxygen in the reaction and inhibited the formation of carbon or Fe_3C. The best OC with $Fe_2O_3/CeO_2/Al_2O_3$ ratio of 65/5/30 OCs achieved the best hydrogen productivity, while the overall performance only decreased by 21% during eighth cycles.

Based on thermodynamic analysis and packed bed experiments, Aston et al. [160] found that the conversion of syngas reached more than 99% during the reduction process of $NiFe_2O_4$ and $CoFe_2O_4$. Furthermore, the reduced $NiFe_2O_4$ (NiFe alloy) and $CoFe_2O_4$ (CoFe alloy) was highly reactive towards water-splitting with regeneration of spinel structure, which rendered the $NiFe_2O_4$ and $CoFe_2O_4$, bearing better redox performance than Fe_2O_3 (not recovered by water) for SCL process. He et al. [161] investigated the effect of preparation methods, including solid-state method, coprecipitation method, hydrothermal method, and sol-gel method, on the SCL performance of $NiFe_2O_4$ nanoparticles. It was found that the OC prepared by sol-gel method displayed the best hydrogen yield and highest lattice oxygen recovery degree due to its smaller particle size and porous structure. Furthermore, further mechanical mixing of $NiFe_2O_4$ and inert SiO_2 could effectively restrain the sintering of $NiFe_2O_4$, rendering outstanding redox stability at 850 °C for 20 cycles. Scheffe et al. [162] prepared m-ZrO_2 (surface area of 50 m^2/g) supported $Co_{0.85}Fe_{2.15}O_4$ via atomic layer deposition (ALD) method and found that such OC produced much more hydrogen than that over γ-Fe_2O_3/m-ZrO_2 in 7 cycles. Mechanism studies suggested that the high yield of hydrogen was ascribed to the deep reduction of Fe/Co cations into CoFe alloy, exceeding the reduction degree of γ-Fe_2O_3 (γ-$Fe_2O_3 \rightarrow$FeO), which improved the oxygen capacity and water-splitting reactivity, and thus, the hydrogen productivity (Figure 14).

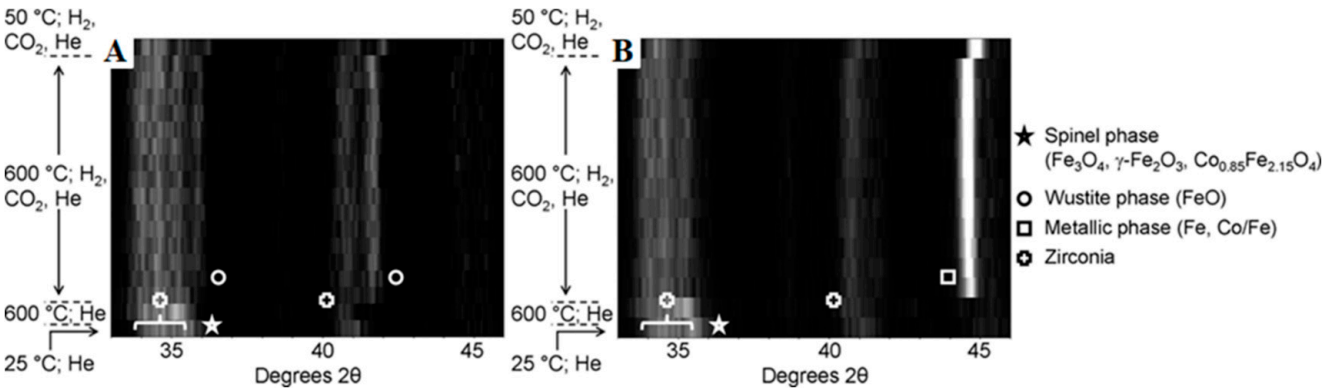

Figure 14. In situ XRD profiles of OCs reduced by 1 vol % H_2/1 vol % CO_2 in He at 600 °C. (**A**) Fe_2O_3 supported on m-ZrO_2 (ALD/20.2% mass loading) and (**B**) $Co_{0.85}Fe_{2.15}O_4$ supported on m-ZrO_2 (ALD/19% mass loading). Chemical reduction for 148 min. Adapted with permission from Ref. [162], copyright 2011, American Chemical Society.

2.5. Photo-Thermochemical Cycle

In 2016, Zhang and coworkers [34] first proposed a strategy of photo-thermochemical cycle (PTC) for CLWS, which explored the photochemical reduction method instead of thermal reduction. This method not only considerably decreased the threshold for abstracting lattice oxygen from OC, slowed down the sintering process, and improved the cyclic stability, but also enabled transformation of solar energy into chemical energy. In a typical photo-thermochemical cycle for water-splitting, the OCs were firstly reduced using ultraviolet and visible light at room temperature with releasing oxygen to generate photo-induced oxygen vacancies, and subsequently recovered by water-splitting via infrared heating to temperature of 500~600 °C with production of hydrogen.

Up to now, the most studied OCs for PTC have been restricted to pure or modified TiO_2 photocatalysts. In 2016, TiO_2 was used as OC for PTC water-splitting to produce hydrogen, and the average hydrogen production of each cycle reached 0.421 mL/g in five consecutive cyclic reactions [34]. However, TiO_2 has a narrow photoresponse range, high recombination rate of photo-induced electron-hole pairs (EHPs), and low reactivity with water. To address these problems, Xu et al. [163] prepared 0.5 wt% Fe/TiO_2 as an OC, which displayed much higher hydrogen yield of 33.36 × 10^{-3} mmol/g than TiO_2 (18.79 × 10^{-3} mmol/g). This is ascribed to the lower recombination rate of EHPs (Figure 15A) and wider photoresponse range (Figure 15B) after doping Fe (III) cations. Further DFT calculations showed that introduction of Fe cations could reduce the oxygen vacancy formation energy, improve H_2O adsorption, and enhance the desorption of generated H_2, which substantially boosted the efficiency of H_2 production (Figure 15C). Docao et al. [164] reported that doping Cu in TiO_2 could raise the distortion degree of TiO_6 octahedron, which improved the oxygen mobility and promoted water-splitting at 140 °C, with solar energy conversion efficiency reaching 0.63%.

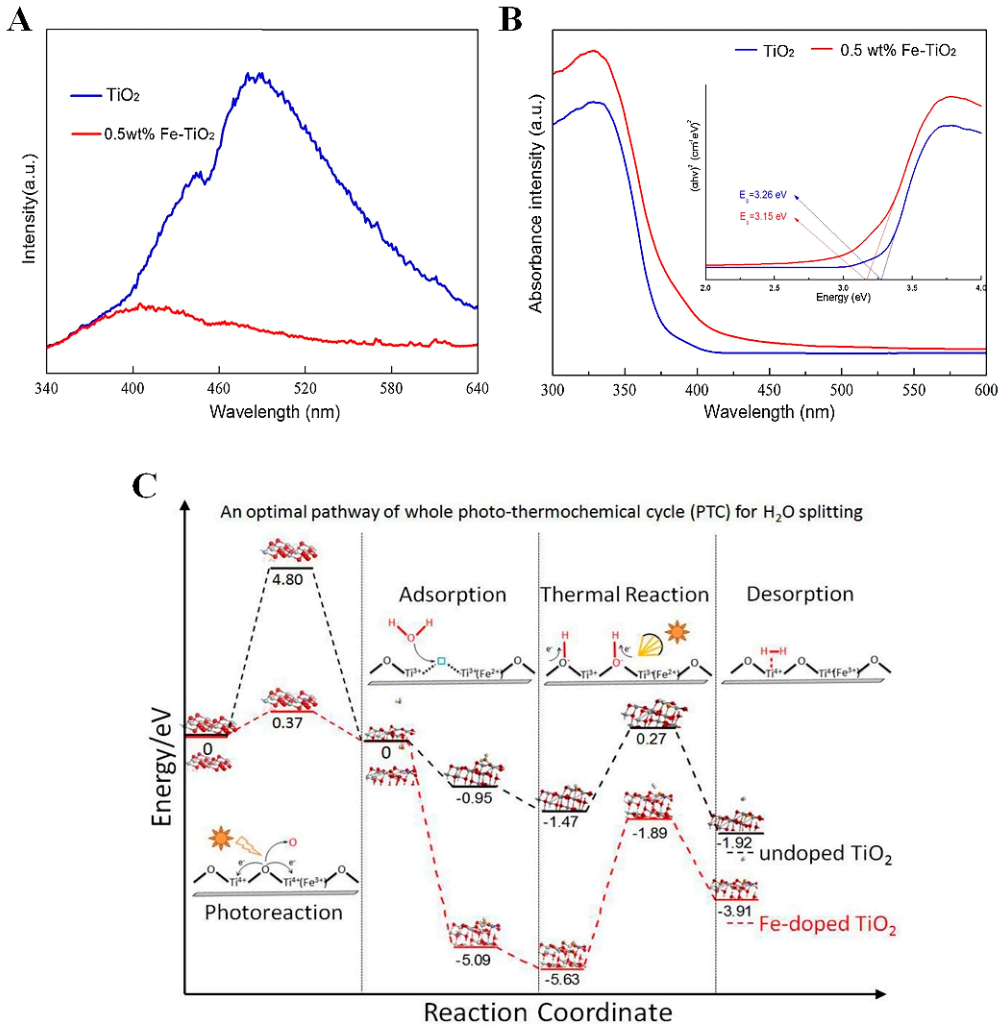

Figure 15. (**A**) PL profiles for TiO_2 and 0.5 wt% Fe-doped TiO_2. (**B**) UV–vis DRS profiles for TiO_2 and 0.5 wt% Fe-doped TiO_2. Inset shows the optical energy band gap. (**C**) The reaction pathway of H_2O splitting during PTC process. Reprinted with permission from Ref. [163], copyright 2017, Elsevier.

Wu et al. [165] modified TiO_2 OCs by doping various transition metals, including Fe, Cu, Co, Ni, and Zn, and discovered that these modified OCs showed higher oxygen vacancy concentration and wider photoresponse range than bare TiO_2. Among these OCs, Cu-doped TiO_2 displayed the highest light absorption rage and the lowest recombination

rate of EHPs, which notably improved the driving force for the release of lattice oxygen and hydrogen production. Further decoration of Cu/TiO_2 by Ni could generate more oxygen vacancies and enhance the activity for water-splitting, which exhibited the maximum hydrogen output of 27.01×10^{-3} mmol/g, nearly 36.0 times higher than that of undoped TiO_2 (0.75×10^{-3} mmol/g) (Figure 16). The follow-up research showed that 0.1~2.0 wt% of Ni-promoted Cu/TiO_2 could anchor nickel oxides (Ni_2O_3 and NiO) around the surface oxygen vacancy while the low valent state NiO showed more pronounced promotion effect towards water-splitting, which rendered the 0.5 wt% Ni-promoted Cu/TiO_2 with highest NiO content, displaying a hydrogen yield (30.6×10^{-3} mmol/g) 40 times higher than that of undoped TiO_2 [166].

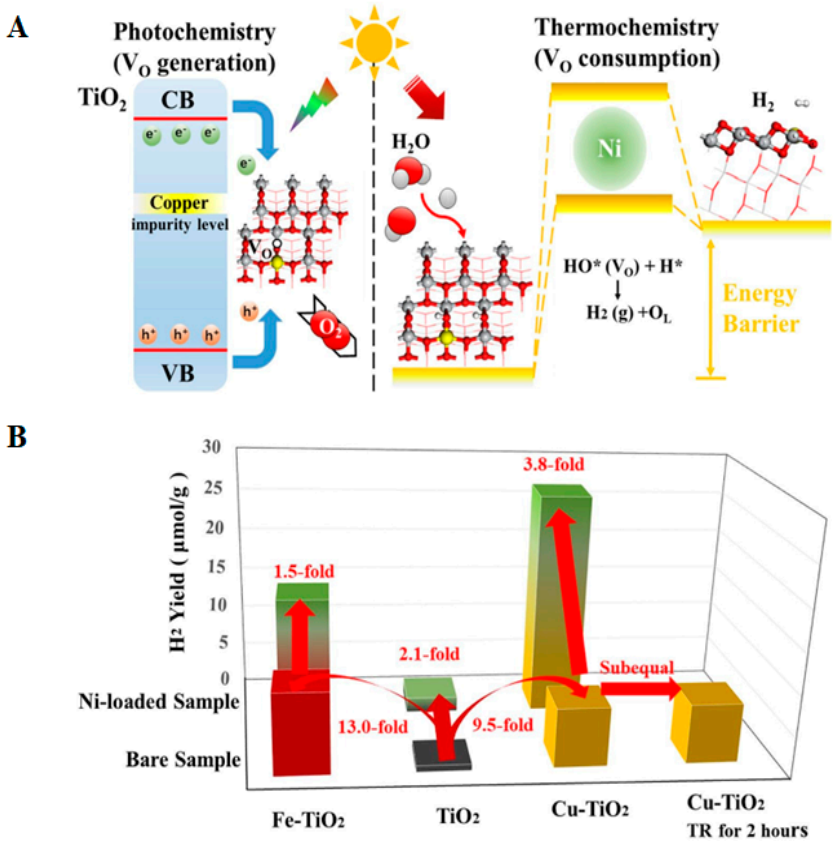

Figure 16. (**A**) Schematic of the reaction mechanism for photochemical and thermochemical processes. (**B**) The average H_2 yield of different catalysts. TR represented "thermochemical reaction". Reprinted with permission from Ref. [165], copyright 2021, Elsevier.

3. Summary and Outlook

Chemical looping water-splitting is promising for sustainable hydrogen production due to the virtue of decoupling a one-step reaction into two or three spatially separated reactions, which greatly simplifies the gas separation process and avoids the harsh conditions for direct water decomposition. To date, different processes have been developed, including a two-step thermochemical water-splitting (TCWS) cycle, methane chemical looping process, chemical looping water gas shift (CL-WGS) cycle, syngas chemical looping (SCL) process, and photo-thermochemical cycle (PTC), with attempts to reduce the energy penalty and CO_2 emissions by altering the method to abstract the lattice oxygen from the OCs, wherein the key lies in the manufacture of suitable OCs. Over the past decades, thousands of metal oxides, such as iron-based metal oxides, zinc-based metal oxides, cerium-based metal oxides, titanium-based metal oxides, and composite metal oxides (perovskite, spinel and garnets, etc.), have been prepared for chemical looping reactions. The performance summary of OCs in different processes of CLWS is summarized in Table 1.

Table 1. Performance summary of OCs in different processes in CLWS.

Hydrogen Production Processes		OCs Type	Cyclic Reaction	OCs	Reaction Temperature (°C; Red/Ox)	H_2 Yield (mmol/g)	Ref.
Two-step TCWS cycle		Ferrites ($M_xFe_{3-x}O_4$)	$M_xFe_{3-x}O_4 \rightarrow xMO + (3-x)FeO + 0.5O_2$; $xMO + (3-x)\,FeO + H_2O \rightarrow M_xFe_{3-x}O_4 + H_2$	$NiFe_2O_4$	1200/800	0.0197 *	[48]
				$Co_{0.67}Fe_{2.33}O_4/ZrO_2$	1300~1400/1000	0.357~0.535	[49]
				$NiFe_2O_4$	1400/1000	~0.446	[50]
				$NiFe_2O_4$/m-ZrO_2	1400/1000	0.535~0.714	[50]
		ZnO_2	$ZnO \rightarrow Zn + O_2$; $Zn + H_2O \rightarrow ZnO + H_2$	ZnO	-	-	
		Cerium oxide ($Ce_xM_{1-x}O_2$)	$Ce_xM_{1-x}O_2 \rightarrow Ce_xM_{1-x}O_{2-\delta} + 0.5\delta\ O_2$; $Ce_xM_{1-x}O_{2-\delta} + H_2O \rightarrow \delta H_2O \rightarrow Ce_xM_{1-x}O_2 + \delta H_2$	CeO_2	1350/800	0.032	[31]
				CeO_2	1500/500	0.142 *	[66]
				$Ce_{0.9}Hf_{0.1}O_2$	1500/500	0.2 *	[66]
				$Ce_{0.9}Sc_{0.1}O_{1.95}$	1500/500	0.181 *	[66]
				$Ce_{0.75}Zr_{0.25}O_2$	1400/1050	0.297	[69]
				1% Gd/CeO_2-ZrO_2	1400/1050	0.338 *	[71]
				CeO_2-0.15SnO_2	1400/800	0.321 *	[72]
				CeO_2	1350/850	0.05	[76]
				CeO_2	1500/1000	0.22	[76]
		ABO_3	$ABO_3 \leftrightarrow ABO_{3-\delta} + 0.5\delta O_2$; $ABO_{3-\delta} + \delta H_2O \rightarrow ABO_3 + \delta H_2$	$LaGa_{0.4}Co_{0.6}O_{3-\delta}$	1350/800	0.478	[31]
				$Sr_{0.4}La_{0.6}Mn_{0.6}Al_{0.4}O_3$	1350/1000	0.307	[75]
				$Sr_{0.4}La_{0.6}Mn_{0.6}Al_{0.4}O_{3-\delta}$	1350/850	0.194	[76]
				$BaCe_{0.25}Mn_{0.75}O_{3-\delta}$	1350/850	0.140	[76]
				$CaTi_{0.5}Mn_{0.5}O_{3-\delta}$	1350/1150	0.446	[78]
	Three reactors chemical looping (M-TRCL)	Iron oxides (Fe_2O_3)	$Fe_2O_3 + CH_4 \rightarrow FeO + 3CO_2 + 2H_2O$; $3FeO + H_2O \rightarrow Fe_3O_4 + H_2$; $2Fe_3O_4 + 0.5O_2 \rightarrow 3Fe_2O_3$	K promoted-Fe_2O_3/Al_2O_3	850/850	-	[97]
				$Fe_2O_3/La_{0.8}Sr_{0.2}FeO_3$	900/900	-	[98]
				$Ce_{0.5}Fe_{0.5}O_{2-\delta}$	850/850	3.71	[87]
Methane chemical looping process	CL-SMR	Cerium oxide ($Ce_xM_{1-x}O_2$)	$Ce_xM_{1-x}O_2 + \delta CH_4 \rightarrow Ce_xM_{1-x}O_{2-\delta} + \delta CO + 2\delta H_2$; $Ce_xM_{1-x}O_{2-\delta} + \delta H_2O \rightarrow Ce_xM_{1-x}O_2 + \delta H_2$	5Ni/CeO_2-TiO_2	900/900	2.098 *	[108]
				CeO_2-Fe_2O_3 (Ce/Fe = 7/3)	850/700	1.116	[109]
				40 wt% Ce-Fe-Zr-O/MgAl-LDO	850/850	1.0	[111]
				CeO_2-$LaFeO_3$	800/800	3.38	[112]
				CeO_2/ZrO_2	800/800	1.736	[114]
		ABO_3	$ABO_3 + \delta CH_4 \rightarrow ABO_{3-\delta} + \delta CO + 2\delta H_2$; $ABO_{3-\delta} + \delta H_2O \rightarrow ABO_3 + \delta H_2$	$LaCo_{0.6}Fe_{0.4}O_3$	700/700	2.22	[117]
				$La_{0.5}Ce_{0.5}FeO_3$	925/925	0.6	[118]
				$La_{0.85}MnFe_{0.15}O_3$	850/850	1.76	[122]
	CL-WGS	Iron oxides (Fe_2O_3)	$Fe_2O_3 + 3CO \rightarrow 2Fe + 3CO_2$; $3Fe + 4H_2O \rightarrow Fe_3O_4 + 4H_2$; $2Fe_3O_4 + 0.5O_2 \rightarrow 3Fe_2O_3$	Fe_2O_3/SiO_2	900/900	~0.745 *	[135]
				Fe_2O_3/Al_2O_3	900/900	~0.982 *	[135]
				Fe_2O_3/YSZ	900/900	~2.232 *	[135]
				Fe_2O_3/ZrO_2	900/900	~2.977 *	[135]
				$Fe_2O_3/MgAl_2O_4$	900/900	2.41~4.152 *	[135]
				Na-modified Fe_2O_3/Al_2O_3	800/800	~13.3	[136]
				Fe_2O_3/ZrO_2	850/850	~7.143 *	[137]
				Fe_2O_3/CeO_2	850/850	~5.80 *	[137]
				$Fe_2O_3/Ce_{0.6}Sm_{0.15}Zr_{0.25}O_{1.925}$	850/850	2.422 *	[139]

Table 1. *Cont.*

Hydrogen Production Processes	OCs Type	Cyclic Reaction	OCs	Reaction Temperature (°C; Red/Ox)	H_2 Yield (mmol/g)	Ref.
SCL process	Iron spinels ($M_xFe_{3-x}O_4$)	$M_xFe_{3-x}O_4 + (2-x)H_2 + CO \rightarrow xMO + (3-x)Fe + CO_2 + (3-x)H_2O$; $Fe + H_2O \rightarrow Fe_3O_4 + H_2$; $xMO + (3-x)/3Fe_3O_4 + 0.5xO_2 \rightarrow M_xFe_{3-x}O_4$	3.3 wt% Al-modified $NiFe_2O_4$	800/800	8.2	[143]
			$ZnFeAlO_x$	850/850	2.23	[144]
			$CoFe_2O_4$	650/650	11.9	[145]
			$Cu_{0.25}Co_{0.25}Fe_{2.5}O_4$	550/550	~11.9	[146]
	Brownmillerite ($Ca_2Fe_2O_5$)	$Ca_2Fe_2O_5 + 3CO \rightarrow 2CaO + 2Fe + 3CO_2$; $2CaO + 2Fe + 3H_2O \rightarrow Ca_2Fe_2O_5 + 3H_2$	$Ca_2Fe_2O_5$	900/900	-	[149]
	Iron oxides (Fe_2O_3)	$Fe_2O_3 + 2H_2 + CO \rightarrow 2Fe + CO_2 + 2H_2O$ $3Fe + 4H_2O \rightarrow Fe_3O_4 + 4H_2$; $2Fe_3O_4 + 0.5O_2 \rightarrow 3Fe_2O_3$	Fe-Ce-Ni based OCs (Ce/Ni/Fe ratio of 10/3/100)	750/750	11.79	[158]
			Fe_2O_3	600/600	1.14	[162]
	Iron spinels ($M_xFe_{3-x}O_4$)	$M_xFe_{3-x}O_4 + CO \rightarrow xMO + (3-x)Fe + CO_2$; $xMO + (3-x)FeO + H_2O \rightarrow M_xFe_{3-x}O_4 + H_2$;	$Co_{0.85}Fe_{2.15}O_4/m\text{-}ZrO_2$	600/600	3.944	[162]
PTC	TiO_2	$2TiO_2 \rightarrow Ti_2O_3 + 0.5O_2$; $Ti_2O_3 + H_2O \rightarrow 2TiO_2 + H_2$ ($hv + TiO_2 \rightarrow e^- + h^+$; $e^- + Ti^{4+} \rightarrow Ti^{3+}$; $h^+ + O_2 \rightarrow O_2 + Vo$; $Vo + H_2O \rightarrow Vo(H_2O)$ $Ti^{3+}\text{-}Vo\ (H_2O)\text{-}Ti^{3+} \rightarrow Ti^{4+}\text{-}O\text{-}Ti^{4+} + H_2$)	TiO_2	room temperature/500-600	0.0188 *	[34]
			0.5 wt% Fe/TiO_2	room temperature/600	0.0334	[163]
			TiO_2	room temperature/350	0.75×10^{-3}	[165]
			Fe/TiO_2	room temperature/350	9.73×10^{-3}	[165]
			Cu/TiO_2	room temperature/350	7.13×10^{-3}	[165]
			Ni-promoted Cu/TiO_2	room temperature/350	0.027	[165]
			0.5% Ni-promoted Cu/TiO_2	room temperature/350	0.0306	[166]

* The unit of raw hydrogen production data is "mL/g", which can be converted into "mmol/g" by the formula PV = nRT with hypothesis of STP condition.

For the two-step TCWS cycle, various OCs, such as iron oxides, zinc oxides, cerium oxides, and perovskite have been widely studied. Among them, cerium oxides have attracted particular attention due to their high structural stability and water-splitting conversion. However, the relatively low reduction degree during the redox cycle, rendering a low hydrogen yield (0.72~7.58 mL/g), greatly hampered its practical applications. Recent work showed that perovskite oxides are promising candidates for two-step TCWS with hydrogen yields of up to 3.13 to 10.71 mL/g, since their redox properties can be facilely modulated by tuning the A/B sites. This gives a clue that constructing composite materials to adjust the redox potential suitable for oxygen desorption and water-splitting should be the key for improving the hydrogen productivity. Furthermore, the sintering problems, thermal shocks, and long single redox cycle time, induced by application of high thermal reduction temperature and low water-splitting temperature, represents another huge obstacle for commercialization of this process. Therefore, introducing support to stabilize the OCs and exploring isothermal redox reactions would be effective in improving the process efficiency for hydrogen production.

Compared to the two-step TCWS cycle, introducing reducing gas, such as methane, carbon monoxide, and syngas, to reduce the oxygen carrier is capable of notably decreasing the reaction temperature to below 1000 °C while enhancing the available oxygen capacity, which significantly decreases the energy consumption, slows down the sintering of OCs, and improve the yield of hydrogen to 13.44~267.63 mL/g. As for methane-driven reduction, valuable syngas with H_2/CO ratio of two for Fischer–Tropsch synthesis and methanol production is produced when a suitable OC is selected. Upon OCs with high reducibility applied, the reducing gaseous can be totally combusted with generation of high concentration CO_2 (and H_2O). All these processes greatly inhibit the side reactions and reduce the burden for gas separation and CO_2 caption, rendering improved efficiency and lowered cost for hydrogen production. Among the investigated OCs, iron-based oxides are among the most studied materials due to the virtues of low-cost, environmentally benign features with the high capacity to donate lattice oxygen by varying the valence state of Fe cations. Herein, the relatively low reactivity of iron cations towards conversion of these reducing agents and general trade-off between selectivity and hydrogen yield represent the main challenge for widespread application of these techniques. For CL-SMR with the aim of methane partial oxidation, the reactivity for C–H bond cleavage can be improved by introducing reactive promoters (e.g., Ni and Cu), creating oxygen vacancies, and engineering the morphology of OCs to provide more active centers. To break the trade-off between selectivity and hydrogen productivity, the key lies in a balance between oxygen supply and methane decomposition, which sustainably restrains the coke formation and increases the oxygen capacity for water-splitting. Based on available results, constructing OCs with core-shell structure, composite oxides, and poisoning active Fe^0 by forming an alloy or covering with oxides are effective methods to inhibit the carbon deposition. When total combustion of reducing agents (processes of methane-driven three step CLWS, CL-WGS, and SCL) is desired, the reduction degree of OC and hydrogen productivity can be improved by introducing MIEC support, alkali promoters, and some active metals (e.g., Co and Cu), which contribute to promote oxygen mobility and oxygen capacity.

In the case of PTC cycle, the reduction of OCs was realized at ambient temperature with hydrogen production at low temperature (140~600 °C), which greatly suppressed the sintering of OCs. More importantly, the solar energy can be well converted to chemical energy, implementing production of green hydrogen. Up to now, the studied OCs are still limited to bare or modified titanium oxide. Although much progress has been achieved in restraining the recombination rate of EHPs and enhancing the reactivity towards water-splitting, which resulted in improved redox performance, the hydrogen yield (0.0168~0.685 mL/g) is still lower than the above CLWS process, because the photo-driven reduction mainly drives the surface lattice oxygen desorption of OCs, and the amount of desorbed oxygen desorption is limited. In addition to exploring advanced OCs that release more oxygen in the photothermal reduction process, it is anticipated that a combination

of suitable reducing gas and photothermal reduction would be promising to significantly enhance the efficiency of hydrogen production.

Over the past 30 years, great effort has been made to develop various OCs by engineering the composition of oxides, including simple metal oxides (cerium oxides, iron oxides, titanium oxides, etc.), composite metal oxides (e.g., perovskite, spinel and garnets), and mixed oxides (e.g., supported OCs, Fe_2O_3-CeO_2, and CeO_2-TiO_2), which greatly improved the redox performance in CLWS processes [31,48,58,97,104,108,110,125,145,167]. B In addition, modulating the microstructure during the redox reactions also exerts a big influence on the performance due to the modulating of surface active centers, concentration of oxygen vacancies, or metal–oxygen bond strength. For example, Li et al. [124] prepared a kind of Fe_2O_3@$La_xSr_{1-x}FeO_{3-\delta}$ (LSF) OC with core-shell structure and showed that the LSF shell with high methane-to-syngas selectivity could reduce the contact between methane and Fe_2O_3, which enables a high CO selectivity above 98%, while the Fe_2O_3 core can donate oxygen to the LSF shell that greatly enhances the oxygen capacity of this OC. Qian et al. [78] found that the crystal phase of $CaTi_{0.5}Mn_{0.5}O_{3-\delta}$ OCs could change from an orthogonal phase to a cubic phase during the thermal reduction process, which greatly promoted the desorption of lattice oxygen. Furthermore, the OCs with cubic phase integrate the virtues of high entropy and medium enthalpy, which improves the reactivity for hydrogen production via water-splitting. Wang et al. [121] demonstrated that a specific Fe^0@ oxide mediate with core-shell structure was formed when $La_{0.6}Sr_{0.4}Fe_{0.8}Al_{0.2}O_{3-\delta}$ was reduced by methane, which notably reduced the direct contact between methane and generated Fe^0 species, restrained the coke deposition, and improved the syngas productivity. Cui et al. [144] indicated that the active component (Fe) of $ZnFeAlO_x$ OCs reversibly exsolved and dissolved from the interface structure of Zn-Fe-Al-O mixed spinel during a CL-WGS process, which can effectively hinder the migration and agglomeration of iron ions and avoid sintering of materials. These results clearly indicate that adjusting the structure changes during redox reactions represents an effective method to modulate the redox performance for CLWS processes.

At present, selection of OCs for CLWS reactions mainly relies on screening method. This is mainly ascribed to the harsh reaction conditions and dynamic structural evolution during redox reactions, which poses a huge challenge for comprehensively understanding the reaction mechanism and designing advanced OCs for CLWS reactions. Future studies should pay more attention to establish a more precise structure–function relationship with the help of in situ characterization, theoretical calculations, and thermodynamic analysis to provide a theoretical basis and development direction for the design of new efficient long-life OCs. Furthermore, according to the pioneering studies, the research focus of OCs is gradually transferred from simple metal oxides to composite oxides (e.g., perovskite) and mixed oxides due to the feasibility of modulating the redox properties by altering the composition of OCs or synergy between different oxides, which bypasses the shortcomings of single metal oxides, and improves the performance of hydrogen production. Therefore, exploring composite oxides to precisely control the metal–oxygen bond strength and mixed oxides to integrate the advantages of different oxides would be an effective strategy for further improving the redox performance of OCs.

Author Contributions: Conceptualization, writing—original draft preparation, W.C.; writing—review and editing, Y.H. (Yue Hu) and W.X.; supervision, writing—review and editing, C.H.; investigation, H.C.; investigation, J.H.; resources, Y.H. (Yujia Han); supervision, writing—review and editing, Y.Z.; resources, X.M.; supervision, X.W. All authors have read and agreed to the published version of the manuscript.

Funding: National Natural Science Foundation of China (No. 21706254, 21978239, and 22178337), Joint Fund of the Yulin University and the Dalian National Laboratory for Clean Energy (No. 2021012), and the Cyrus Tang Foundation are gratefully acknowledged.

Conflicts of Interest: The authors declare no conflict of interest.

References

1. Bockris, J. The origin of ideas on a Hydrogen Economy and its solution to the decay of the environment. *Int. J. Hydrogen Energy* **2002**, *27*, 731–740. [CrossRef]
2. Safari, F.; Dincer, I. A review and comparative evaluation of thermochemical water splitting cycles for hydrogen production. *Energy Convers. Manag.* **2020**, *205*, 112182. [CrossRef]
3. Alves, H.J.; Bley Junior, C.; Niklevicz, R.R.; Frigo, E.P.; Frigo, M.S.; Coimbra-Araújo, C.H. Overview of hydrogen production technologies from biogas and the applications in fuel cells. *Int. J. Hydrogen Energy* **2013**, *38*, 5215–5225. [CrossRef]
4. Dincer, I.; Acar, C. Review and evaluation of hydrogen production methods for better sustainability. *Int. J. Hydrogen Energy* **2015**, *40*, 11094–11111. [CrossRef]
5. Mahant, B.; Linga, P.; Kumar, R. Hydrogen Economy and Role of Hythane as a Bridging Solution: A Perspective Review. *Energy Fuels* **2021**, *35*, 15424–15454. [CrossRef]
6. Navarro, R.M.; Pena, M.A.; Fierro, J.L. Hydrogen production reactions from carbon feedstocks: Fossil fuels and biomass. *Chem. Rev.* **2007**, *107*, 3952–3991. [CrossRef]
7. Go, K.S.; Son, S.R.; Kim, S.D.; Kang, K.S.; Park, C.S. Hydrogen production from two-step steam methane reforming in a fluidized bed reactor. *Int. J. Hydrogen Energy* **2009**, *34*, 1301–1309. [CrossRef]
8. Lee, K.B.; Beaver, M.G.; Caram, H.S.; Sircar, S. Novel Thermal-Swing Sorption-Enhanced Reaction Process Concept for Hydrogen Production by Low-Temperature Steam–Methane Reforming. *Ind. Eng. Chem. Res.* **2007**, *46*, 5003–5014. [CrossRef]
9. Wang, J.; Sakanishi, K.; Saito, I.; Takarada, T.; Morishita, K. High-Yield Hydrogen Production by Steam Gasification of HyperCoal (Ash-Free Coal Extract) with Potassium Carbonate: Comparison with Raw Coal. *Energy Fuels* **2005**, *19*, 2114–2120. [CrossRef]
10. Wang, Z.; Li, L.; Zhang, G. Life cycle greenhouse gas assessment of hydrogen production via chemical looping combustion thermally coupled steam reforming. *J. Clean. Prod.* **2018**, *179*, 335–346. [CrossRef]
11. Li, J.; Cheng, W. Comparative life cycle energy consumption, carbon emissions and economic costs of hydrogen production from coke oven gas and coal gasification. *Int. J. Hydrogen Energy* **2020**, *45*, 27979–27993. [CrossRef]
12. Zhang, H.; Sun, Z.; Hu, Y.H. Steam reforming of methane: Current states of catalyst design and process upgrading. *Renew. Sust. Energy Rev.* **2021**, *149*, 111330. [CrossRef]
13. Siefert, N.S.; Shekhawat, D.; Litster, S.; Berry, D.A. Steam–Coal Gasification Using CaO and KOH for in Situ Carbon and Sulfur Capture. *Energy Fuels* **2013**, *27*, 4278–4289. [CrossRef]
14. Kodama, T.; Gokon, N. Thermochemical cycles for high-temperature solar hydrogen production. *Chem. Rev.* **2007**, *107*, 4048–4077. [CrossRef]
15. Kogan, A. Direct solar thermal splitting of water and on-site separation of the products-II. Experimental feasibility study. *Int. J. Hydrogen Energy* **1998**, *23*, 89–98. [CrossRef]
16. Bilgen, E.; Ducarroir, M.; Foex, M.; Sibieude, F.; Trombe, F. Use of solar energy for direct and two-step water decomposition cycles. *Int. J. Hydrogen Energy* **1977**, *2*, 251–257. [CrossRef]
17. Marwat, M.A.; Humayun, M.; Afridi, M.W.; Zhang, H.; Abdul Karim, M.R.; Ashtar, M.; Usman, M.; Waqar, S.; Ullah, H.; Wang, C.; et al. Advanced Catalysts for Photoelectrochemical Water Splitting. *ACS Appl. Energy Mater.* **2021**, *4*, 12007–12031. [CrossRef]
18. Zhou, R.; Li, D.; Qu, B.; Sun, X.; Zhang, B.; Zeng, X.C. Rutile TiO_2(011)-2 × 1 Reconstructed Surfaces with Optical Absorption over the Visible Light Spectrum. *ACS Appl. Mater. Interfaces* **2016**, *8*, 27403–27410. [CrossRef] [PubMed]
19. Anpo, M.; Li, J.; Liu, W.; Qi, W.; Song, F. Hydrogen production technology by electrolysis of water and its application in renewable energy consumption. In Proceedings of the 3rd International Conference on Energy Resources and Sustainable Development (ICERSD 2020), Incheon, Republic of Korea, 13–14 January 2020.
20. Laguna-Bercero, M.A. Recent advances in high temperature electrolysis using solid oxide fuel cells: A review. *J. Power Sources* **2012**, *203*, 4–16. [CrossRef]
21. Xue, F.; Su, J.; Li, P.; Zhang, Y. Application of Proton Exchange Membrane Electrolysis of Water Hydrogen Production Technology in Power Plant. In Proceedings of the 3rd International Conference on Air Pollution and Environmental Engineering, Xi'an, China, 28–29 September 2020.
22. Megía, P.J.; Vizcaíno, A.J.; Calles, J.A.; Carrero, A. Hydrogen Production Technologies: From Fossil Fuels toward Renewable Sources. A Mini Review. *Energy Fuels* **2021**, *35*, 16403–16415. [CrossRef]
23. Li, D.; Xu, R.; Li, X.; Li, Z.; Zhu, X.; Li, K. Chemical Looping Conversion of Gaseous and Liquid Fuels for Chemical Production: A Review. *Energy Fuels* **2020**, *34*, 5381–5413. [CrossRef]
24. Moghtaderi, B. Review of the Recent Chemical Looping Process Developments for Novel Energy and Fuel Applications. *Energy Fuels* **2011**, *26*, 15–40. [CrossRef]
25. De Vos, Y.; Jacobs, M.; Van Der Voort, P.; Van Driessche, I.; Snijkers, F.; Verberckmoes, A. Development of Stable Oxygen Carrier Materials for Chemical Looping Processes—A Review. *Catalysts* **2020**, *10*, 926. [CrossRef]
26. Funk, J.E.; Reinstrom, R.M. Energy Requirements in Production of Hydrogen from Water. *Ind. Eng. Chem. Process* **1966**, *5*, 336–342. [CrossRef]
27. Krenzke, P.T.; Fosheim, J.R.; Davidson, J.H. Solar fuels via chemical-looping reforming. *Sol. Energy* **2017**, *156*, 48–72. [CrossRef]
28. Kang, K.-S.; Kim, C.-H.; Bae, K.-K.; Cho, W.-C.; Kim, S.-H.; Park, C.-S. Oxygen-carrier selection and thermal analysis of the chemical-looping process for hydrogen production. *Int. J. Hydrogen Energy* **2010**, *35*, 12246–12254. [CrossRef]

29. Kim, Y.; Lim, H.S.; Kim, H.S.; Lee, M.; Lee, J.W.; Kang, D. Carbon dioxide splitting and hydrogen production using a chemical looping concept: A review. *J. CO_2 Util.* **2022**, *63*, 102139. [CrossRef]
30. Zhao, L.; Dou, B.; Zhang, H.; Wang, Z. Oxygen carriers for chemical-looping water splitting to hydrogen production: A critical review. *Carbon Capture Sci. Technol.* **2021**, *1*, 100006. [CrossRef]
31. Chen, Z.; Jiang, Q.; Cheng, F.; Tong, J.; Yang, M.; Jiang, Z.; Li, C. Sr- and Co-doped $LaGaO_{3-\delta}$ with high O_2 and H_2 yields in solar thermochemical water splitting. *J. Mater. Chem. A* **2019**, *7*, 6099–6112. [CrossRef]
32. de Leeuwe, C.; Hu, W.; Evans, J.; von Stosch, M.; Metcalfe, I.S. Production of high purity H_2 through chemical-looping water–gas shift at reforming temperatures—The importance of non-stoichiometric oxygen carriers. *Chem. Eng. J.* **2021**, *423*, 130174. [CrossRef]
33. Gupta, P.; Velazquez-Vargas, L.G.; Fan, L.-S. Syngas Redox (SGR) Process to Produce Hydrogen from Coal Derived Syngas. *Energy Fuels* **2007**, *21*, 2900–2908. [CrossRef]
34. Zhang, Y.; Chen, J.; Xu, C.; Zhou, K.; Wang, Z.; Zhou, J.; Cen, K. A novel photo-thermochemical cycle of water-splitting for hydrogen production based on TiO_{2-x}/TiO_2. *Int. J. Hydrogen Energy* **2016**, *41*, 2215–2221. [CrossRef]
35. Li, F.; Fan, L.-S. Clean coal conversion processes—Progress and challenges. *Energy Environ. Sci.* **2008**, *1*, 248–267. [CrossRef]
36. Adanez, J.; Abad, A.; Garcia-Labiano, F.; Gayan, P.; de Diego, L.F. Progress in Chemical-Looping Combustion and Reforming technologies. *Prog. Energy Combust. Sci.* **2012**, *38*, 215–282. [CrossRef]
37. Zhu, X.; Imtiaz, Q.; Donat, F.; Müller, C.R.; Li, F. Chemical looping beyond combustion—A perspective. *Energy Environ. Sci.* **2020**, *13*, 772–804. [CrossRef]
38. Zeng, L.; Cheng, Z.; Fan, J.A.; Fan, L.-S.; Gong, J. Metal oxide redox chemistry for chemical looping processes. *Nat. Rev. Chem.* **2018**, *2*, 349–364. [CrossRef]
39. Qasim, M.; Ayoub, M.; Ghazali, N.A.; Aqsha, A.; Ameen, M. Recent Advances and Development of Various Oxygen Carriers for the Chemical Looping Combustion Process: A Review. *Ind. Eng. Chem. Res.* **2021**, *60*, 8621–8641. [CrossRef]
40. Tian, M.; Wang, C.; Han, Y.; Wang, X. Recent Advances of Oxygen Carriers for Chemical Looping Reforming of Methane. *ChemCatChem* **2021**, *13*, 1615–1637. [CrossRef]
41. Li, D.; Xu, R.; Gu, Z.; Zhu, X.; Qing, S.; Li, K. Chemical-Looping Conversion of Methane: A Review. *Energy Technol.* **2019**, *8*, 1900925. [CrossRef]
42. Voitic, G.; Hacker, V. Recent advancements in chemical looping water splitting for the production of hydrogen. *RSC Adv.* **2016**, *6*, 98267–98296. [CrossRef]
43. Luo, M.; Yi, Y.; Wang, S.; Wang, Z.; Du, M.; Pan, J.; Wang, Q. Review of hydrogen production using chemical-looping technology. *Renew. Sustain. Energy Rev.* **2018**, *81*, 3186–3214. [CrossRef]
44. Abanades, S. Metal Oxides Applied to Thermochemical Water-Splitting for Hydrogen Production Using Concentrated Solar Energy. *ChemEngineering* **2019**, *3*, 63. [CrossRef]
45. Muhich, C.L.; Ehrhart, B.D.; Al-Shankiti, I.; Ward, B.J.; Musgrave, C.B.; Weimer, A.W. A review and perspective of efficient hydrogen generation via solar thermal water splitting. *Wiley Interdiscip. Rev. Energy Environ.* **2016**, *5*, 261–287. [CrossRef]
46. Nakamura, T. Hydrogen production from water utilizing solar heat at high temperatures. *Sol. Energy* **1977**, *19*, 467–475. [CrossRef]
47. Steinfeld, A.; Sanders, S.; Palumbo, R. Design aspects of solar thermochemical engineering—A case study: Two-step water-splitting cycle using the Fe3O4/FeO redox system. *Sol. Energy* **1999**, *65*, 43–53. [CrossRef]
48. Han, S.B.; Kang, T.B.; Joo, O.S.; Jung, K.D. Water splitting for hydrogen production with ferrites. *Sol. Energy* **2007**, *81*, 623–628. [CrossRef]
49. Kodama, T.; Kondoh, Y.; Yamamoto, R.; Andou, H.; Satou, N. Thermochemical hydrogen production by a redox system of ZrO_2-supported Co(II)-ferrite. *Sol. Energy* **2005**, *78*, 623–631. [CrossRef]
50. Kodama, T.; Gokon, N.; Yamamoto, R. Thermochemical two-step water splitting by ZrO_2-supported $Ni_xFe_{3-x}O_4$ for solar hydrogen production. *Sol. Energy* **2008**, *82*, 73–79. [CrossRef]
51. Ishihara, H.; Kaneko, H.; Yokoyama, T.; Fuse, A.; Hasegawa, N.; Tamaura, Y. Hydrogen Production Through Two-Step Water Splitting Using YSZ (Ni,Fe) System for Solar Hydrogen Production. In Proceedings of the ASME 2005 International Solar Energy Conference, Orlando, FL, USA, 6–12 August 2005.
52. Miller, J.E.; Allendorf, M.D.; Diver, R.B.; Evans, L.R.; Siegel, N.P.; Stuecker, J.N. Metal oxide composites and structures for ultra-high temperature solar thermochemical cycles. *J. Mater. Sci.* **2008**, *43*, 4714–4728. [CrossRef]
53. Palumbo, R.; Léde, J.; Boutin, O.; Elorza Ricart, E.; Steinfeld, A.; Möller, S.; Weidenkaff, A.; Fletcher, E.A.; Bielicki, J. The production of Zn from ZnO in a high-temperature solar decomposition quench process—I. The scientific framework for the process. *Chem. Eng. Sci.* **1998**, *53*, 2503–2517. [CrossRef]
54. Weidenkaff, A.; Reller, A.W.; Wokaun, A.; Steinfeld, A. Thermogravimetric analysis of the ZnO/Zn water splitting cycle. *Thermochim. Acta* **2000**, *359*, 69–75. [CrossRef]
55. Ernst, F.; Steinfeld, A.; Pratsinis, S. Hydrolysis rate of submicron Zn particles for solar H_2 synthesis. *Int. J. Hydrogen Energy* **2009**, *34*, 1166–1175. [CrossRef]
56. Lv, M.; Zhou, J.; Yang, W.; Cen, K. Thermogravimetric analysis of the hydrolysis of zinc particles. *Int. J. Hydrogen Energy* **2010**, *35*, 2617–2621. [CrossRef]
57. Abanades, S.; Flamant, G. Thermochemical hydrogen production from a two-step solar-driven water-splitting cycle based on cerium oxides. *Sol. Energy* **2006**, *80*, 1611–1623. [CrossRef]

58. Chueh, W.C.; Falter, C.; Abbott, M.; Scipio, D.; Furler, P.; Haile, S.M.; Steinfeld, A. High-flux solar-driven thermochemical dissociation of CO_2 and H_2O using nonstoichiometric ceria. *Science* **2010**, *330*, 1797–1801. [CrossRef] [PubMed]
59. Costa Oliveira, F.A.; Barreiros, M.A.; Haeussler, A.; Caetano, A.P.F.; Mouquinho, A.I.; Oliveira e Silva, P.M.; Novais, R.M.; Pullar, R.C.; Abanades, S. High performance cork-templated ceria for solar thermochemical hydrogen production via two-step water-splitting cycles. *Sustain. Energy Fuels* **2020**, *4*, 3077–3089. [CrossRef]
60. Singh, P.; Hegde, M.S. $Ce_{0.67}Cr_{0.33}O_{2.11}$: A New Low-Temperature O_2 Evolution Material and H_2 Generation Catalyst by Thermochemical Splitting of Water. *Chem. Mater.* **2009**, *22*, 762–768. [CrossRef]
61. Le Gal, A.; Abanades, S.; Flamant, G. CO_2 and H_2O Splitting for Thermochemical Production of Solar Fuels Using Nonstoichiometric Ceria and Ceria/Zirconia Solid Solutions. *Energy Fuels* **2011**, *25*, 4836–4845. [CrossRef]
62. Chen, Z.; Jiang, Q.; An, H.; Zhang, J.; Hao, S.; Li, X.; Cai, L.; Yu, W.; You, K.; Zhu, X.; et al. Platinum Group Metal Catalyst (RuO_x, PtO_x, and IrO_x)-Decorated Ceria-Zirconia Solid Solution as High Active Oxygen Carriers for Solar Thermochemical CO_2 Splitting. *ACS Catal.* **2022**, *12*, 7719–7736. [CrossRef]
63. Petkovich, N.D.; Rudisill, S.G.; Venstrom, L.J.; Boman, D.B.; Davidson, J.H.; Stein, A. Control of Heterogeneity in Nanostructured $Ce_{1-x}Zr_xO_2$ Binary Oxides for Enhanced Thermal Stability and Water Splitting Activity. *J. Phys. Chem. C* **2011**, *115*, 21022–21033. [CrossRef]
64. Gokon, N.; Suda, T.; Kodama, T. Oxygen and hydrogen productivities and repeatable reactivity of 30-mol%-Fe-, Co-, Ni-, Mn-doped $CeO_{2-\delta}$ for thermochemical two-step water-splitting cycle. *Energy* **2015**, *90*, 1280–1289. [CrossRef]
65. Kaneko, H.; Miura, T.; Ishihara, H.; Taku, S.; Yokoyama, T.; Nakajima, H.; Tamaura, Y. Reactive ceramics of CeO_2–MO_x (M = Mn, Fe, Ni, Cu) for H_2 generation by two-step water splitting using concentrated solar thermal energy. *Energy* **2007**, *32*, 656–663. [CrossRef]
66. Meng, Q.-L.; Lee, C.-i.; Ishihara, T.; Kaneko, H.; Tamaura, Y. Reactivity of CeO_2-based ceramics for solar hydrogen production via a two-step water-splitting cycle with concentrated solar energy. *Int. J. Hydrogen Energy* **2011**, *36*, 13435–13441. [CrossRef]
67. Lee, C.-i.; Meng, Q.-L.; Kaneko, H.; Tamaura, Y. Solar Hydrogen Productivity of Ceria–Scandia Solid Solution Using Two-Step Water-Splitting Cycle. *J. Sol. Energy Eng.* **2013**, *135*, 011002. [CrossRef]
68. Le Gal, A.; Abanades, S.; Bion, N.; Le Mercier, T.; Harlé, V. Reactivity of Doped Ceria-Based Mixed Oxides for Solar Thermochemical Hydrogen Generation via Two-Step Water-Splitting Cycles. *Energy Fuels* **2013**, *27*, 6068–6078. [CrossRef]
69. Le Gal, A.; Abanades, S. Catalytic investigation of ceria-zirconia solid solutions for solar hydrogen production. *Int. J. Hydrogen Energy* **2011**, *36*, 4739–4748. [CrossRef]
70. Abanades, S.; Legal, A.; Cordier, A.; Peraudeau, G.; Flamant, G.; Julbe, A. Investigation of reactive cerium-based oxides for H_2 production by thermochemical two-step water-splitting. *J. Mater. Sci.* **2010**, *45*, 4163–4173. [CrossRef]
71. Le Gal, A.; Abanades, S. Dopant Incorporation in Ceria for Enhanced Water-Splitting Activity during Solar Thermochemical Hydrogen Generation. *J. Phys. Chem. C* **2012**, *116*, 13516–13523. [CrossRef]
72. Ruan, C.; Tan, Y.; Li, L.; Wang, J.; Liu, X.; Wang, X. A novel $CeO_{2-x}SnO_2/Ce_2Sn_2O_7$ pyrochlore cycle for enhanced solar thermochemical water splitting. *AlChE J.* **2017**, *63*, 3450–3462. [CrossRef]
73. Zhu, X.; Li, K.; Neal, L.; Li, F. Perovskites as Geo-inspired Oxygen Storage Materials for Chemical Looping and Three-Way Catalysis: A Perspective. *ACS Catal.* **2018**, *8*, 8213–8236. [CrossRef]
74. Takacs, M.; Hoes, M.; Caduff, M.; Cooper, T.; Scheffe, J.R.; Steinfeld, A. Oxygen nonstoichiometry, defect equilibria, and thermodynamic characterization of $LaMnO_3$ perovskites with Ca/Sr A-site and Al B-site doping. *Acta Mater.* **2016**, *103*, 700–710. [CrossRef]
75. McDaniel, A.H.; Miller, E.C.; Arifin, D.; Ambrosini, A.; Coker, E.N.; O'Hayre, R.; Chueh, W.C.; Tong, J. Sr- and Mn-doped $LaAlO_{3-\delta}$ for solar thermochemical H_2 and CO production. *Energy Environ. Sci.* **2013**, *6*, 2424–2428. [CrossRef]
76. Barcellos, D.R.; Sanders, M.D.; Tong, J.; McDaniel, A.H.; O'Hayre, R.P. $BaCe_{0.25}Mn_{0.75}O_{3-\delta}$—A promising perovskite-type oxide for solar thermochemical hydrogen production. *Energy Environ. Sci.* **2018**, *11*, 3256–3265. [CrossRef]
77. Sai Gautam, G.; Stechel, E.B.; Carter, E.A. Exploring Ca–Ce–M–O (M = 3d Transition Metal) Oxide Perovskites for Solar Thermochemical Applications. *Chem. Mater.* **2020**, *32*, 9964–9982. [CrossRef]
78. Qian, X.; He, J.; Mastronardo, E.; Baldassarri, B.; Yuan, W.; Wolverton, C.; Haile, S.M. Outstanding Properties and Performance of $CaTi_{0.5}Mn_{0.5}O_{3-\delta}$ for Solar-Driven Thermochemical Hydrogen Production. *Matter* **2021**, *4*, 688–708. [CrossRef]
79. Chuayboon, S.; Abanades, S.; Rodat, S. High-Purity and Clean Syngas and Hydrogen Production From Two-Step CH_4 Reforming and H_2O Splitting Through Isothermal Ceria Redox Cycle Using Concentrated Sunlight. *Front. Energy Res.* **2020**, *8*, 00128. [CrossRef]
80. Wang, L.; Ma, T.; Chang, Z.; Li, H.; Fu, M.; Li, X. Solar fuels production via two-step thermochemical cycle based on Fe_3O_4/Fe with methane reduction. *Sol. Energy* **2019**, *177*, 772–781. [CrossRef]
81. He, F.; Li, F. Perovskite promoted iron oxide for hybrid water-splitting and syngas generation with exceptional conversion. *Energy Environ. Sci.* **2015**, *8*, 535–539. [CrossRef]
82. Chuayboon, S.; Abanades, S.; Rodat, S. Syngas production via solar-driven chemical looping methane reforming from redox cycling of ceria porous foam in a volumetric solar reactor. *Chem. Eng. J.* **2019**, *356*, 756–770. [CrossRef]
83. Welte, M.; Warren, K.; Scheffe, J.R.; Steinfeld, A. Combined Ceria Reduction and Methane Reforming in a Solar-Driven Particle-Transport Reactor. *Ind. Eng. Chem. Res.* **2017**, *56*, 10300–10308. [CrossRef] [PubMed]

84. Saha, D.; Grappe, H.A.; Chakraborty, A.; Orkoulas, G. Postextraction Separation, On-Board Storage, and Catalytic Conversion of Methane in Natural Gas: A Review. *Chem. Rev.* **2016**, *116*, 11436–11499. [CrossRef] [PubMed]
85. Olivos-Suarez, A.I.; Szécsényi, À.; Hensen, E.J.M.; Ruiz-Martinez, J.; Pidko, E.A.; Gascon, J. Strategies for the Direct Catalytic Valorization of Methane Using Heterogeneous Catalysis: Challenges and Opportunities. *ACS Catal.* **2016**, *6*, 2965–2981. [CrossRef]
86. He, Y.; Zhu, L.; Li, L.; Liu, G. Hydrogen and Power Cogeneration Based on Chemical Looping Combustion: Is It Capable of Reducing Carbon Emissions and the Cost of Production? *Energy Fuels* **2020**, *34*, 3501–3512. [CrossRef]
87. Zhu, X.; Wei, Y.; Wang, H.; Li, K. Ce–Fe oxygen carriers for chemical-looping steam methane reforming. *Int. J. Hydrogen Energy* **2013**, *38*, 4492–4501. [CrossRef]
88. Zhu, Y.; Liu, W.; Sun, X.; Ma, X.; Kang, Y.; Wang, X.; Wang, J. La-hexaaluminate for synthesis gas generation by Chemical Looping Partial Oxidation of Methane Using CO_2 as Sole Oxidant. *AlChE J.* **2018**, *64*, 550–563. [CrossRef]
89. Shen, Q.; Huang, F.; Tian, M.; Zhu, Y.; Li, L.; Wang, J.; Wang, X. Effect of Regeneration Period on the Selectivity of Synthesis Gas of Ba-Hexaaluminates in Chemical Looping Partial Oxidation of Methane. *ACS Catal.* **2018**, *9*, 722–731. [CrossRef]
90. Krenzke, P.T.; Davidson, J.H. Thermodynamic Analysis of Syngas Production via the Solar Thermochemical Cerium Oxide Redox Cycle with Methane-Driven Reduction. *Energy Fuels* **2014**, *28*, 4088–4095. [CrossRef]
91. Wang, X.; Du, X.; Yu, W.; Zhang, J.; Wei, J. Coproduction of Hydrogen and Methanol from Methane by Chemical Looping Reforming. *Ind. Eng. Chem. Res.* **2019**, *58*, 10296–10306. [CrossRef]
92. Zhang, F.; Zhu, L.; Wang, Y.; Sun, L. Exergy analysis on the process for three reactors chemical looping hydrogen generation. *Int. J. Hydrogen Energy* **2020**, *45*, 24322–24332. [CrossRef]
93. De Vos, Y.; Jacobs, M.; Van Der Voort, P.; Van Driessche, I.; Snijkers, F.; Verberckmoes, A. Sustainable iron-based oxygen carriers for Chemical Looping for Hydrogen Generation. *Int. J. Hydrogen Energy* **2019**, *44*, 1374–1391. [CrossRef]
94. Go, K.; Son, S.; Kim, S. Reaction kinetics of reduction and oxidation of metal oxides for hydrogen production. *Int. J. Hydrogen Energy* **2008**, *33*, 5986–5995. [CrossRef]
95. Kang, K.-S.; Kim, C.-H.; Cho, W.-C.; Bae, K.-K.; Woo, S.-W.; Park, C.-S. Reduction characteristics of $CuFe_2O_4$ and Fe_3O_4 by methane; $CuFe_2O_4$ as an oxidant for two-step thermochemical methane reforming. *Int. J. Hydrogen Energy* **2008**, *33*, 4560–4568. [CrossRef]
96. Ku, Y.; Wu, H.-C.; Chiu, P.-C.; Tseng, Y.-H.; Kuo, Y.-L. Methane combustion by moving bed fuel reactor with Fe_2O_3/Al_2O_3 oxygen carriers. *Appl. Energy* **2014**, *113*, 1909–1915. [CrossRef]
97. Zhu, M.; Chen, S.; Ma, S.; Xiang, W. Carbon formation on iron-based oxygen carriers during CH_4 reduction period in Chemical Looping Hydrogen Generation process. *Chem. Eng. J.* **2017**, *325*, 322–331. [CrossRef]
98. Galinsky, N.L.; Huang, Y.; Shafiefarhood, A.; Li, F. Iron Oxide with Facilitated O^{2-} Transport for Facile Fuel Oxidation and CO_2 Capture in a Chemical Looping Scheme. *ACS Sustain. Chem. Eng.* **2013**, *1*, 364–373. [CrossRef]
99. Fung, V.; Polo-Garzon, F.; Wu, Z.; Jiang, D.-e. Exploring perovskites for methane activation from first principles. *Catal. Sci. Technol.* **2018**, *8*, 702–709. [CrossRef]
100. Mattisson, T.; Lyngfelt, A. Capture of CO_2 using chemical-looping combustion. In Proceedings of the First Biennial Meeting of the Scandinavian-928 Nordic Section of the Combustion Institute, Göteborg, Sweden, 18–20 April 2001.
101. Moghtaderi, B. Hydrogen enrichment of fuels using a novel miniaturised chemical looping steam reformer. *Chem. Eng. Res. Des.* **2012**, *90*, 19–25. [CrossRef]
102. Liu, Y.; Qin, L.; Cheng, Z.; Goetze, J.W.; Kong, F.; Fan, J.A.; Fan, L.S. Near 100% CO selectivity in nanoscaled iron-based oxygen carriers for chemical looping methane partial oxidation. *Nat. Commun.* **2019**, *10*, 5503. [CrossRef] [PubMed]
103. Cheng, Z.; Qin, L.; Guo, M.; Xu, M.; Fan, J.A.; Fan, L.S. Oxygen vacancy promoted methane partial oxidation over iron oxide oxygen carriers in the chemical looping process. *Phys. Chem. Chem. Phys.* **2016**, *18*, 32418–32428. [CrossRef] [PubMed]
104. Kang, Y.; Tian, M.; Huang, C.; Lin, J.; Hou, B.; Pan, X.; Li, L.; Rykov, A.I.; Wang, J.; Wang, X. Improving Syngas Selectivity of Fe_2O_3/Al_2O_3 with Yttrium Modification in Chemical Looping Methane Conversion. *ACS Catal.* **2019**, *9*, 8373–8382. [CrossRef]
105. Li, D.; Li, K.; Xu, R.; Wang, H.; Tian, D.; Wei, Y.; Zhu, X.; Zeng, C.; Zeng, L. $Ce_{1-x}Fe_xO_{2-\delta}$ catalysts for catalytic methane combustion: Role of oxygen vacancy and structural dependence. *Catal. Today* **2018**, *318*, 73–85. [CrossRef]
106. Han, Y.; Tian, M.; Wang, C.; Kang, Y.; Kang, L.; Su, Y.; Huang, C.; Zong, T.; Lin, J.; Hou, B.; et al. Highly Active and Anticoke Ni/CeO_2 with Ultralow Ni Loading in Chemical Looping Dry Reforming via the Strong Metal–Support Interaction. *ACS Sustain. Chem. Eng.* **2021**, *9*, 17276–17288. [CrossRef]
107. Murray, E.P.; Tsai, T.; Barnett, S.A. A direct-methane fuel cell with a ceria-based anode. *Nature* **1999**, *400*, 649–651. [CrossRef]
108. Ruan, C.; Huang, Z.-Q.; Lin, J.; Li, L.; Liu, X.; Tian, M.; Huang, C.; Chang, C.-R.; Li, J.; Wang, X. Synergy of the catalytic activation on Ni and the CeO_2–$TiO_2/Ce_2Ti_2O_7$ stoichiometric redox cycle for dramatically enhanced solar fuel production. *Energy Environ. Sci.* **2019**, *12*, 767–779. [CrossRef]
109. Zhu, X.; Wang, H.; Wei, Y.; Li, K.; Cheng, X. Hydrogen and syngas production from two-step steam reforming of methane over CeO_2-Fe_2O_3 oxygen carrier. *J. Rare Earths* **2010**, *28*, 907–913. [CrossRef]
110. Zhu, X.; Li, K.; Wei, Y.; Wang, H.; Sun, L. Chemical-Looping Steam Methane Reforming over a CeO_2–Fe_2O_3 Oxygen Carrier: Evolution of Its Structure and Reducibility. *Energy Fuels* **2014**, *28*, 754–760. [CrossRef]
111. Yuan, J.; Zhao, Y.; Xu, H.; Lu, C.; Yang, K.; Zhu, X.; Li, K. Layered Mg-Al spinel supported Ce-Fe-Zr-O oxygen carriers for chemical looping reforming. *Chin. J. Chem. Eng.* **2020**, *28*, 2668–2676. [CrossRef]

112. Zheng, Y.; Li, K.; Wang, H.; Tian, D.; Wang, Y.; Zhu, X.; Wei, Y.; Zheng, M.; Luo, Y. Designed oxygen carriers from macroporous $LaFeO_3$ supported CeO_2 for chemical-looping reforming of methane. *Appl. Catal. B* **2017**, *202*, 51–63. [CrossRef]
113. Cheng, Z.; Zhang, L.; Jin, N.; Zhu, Y.; Chen, L.; Yang, Q.; Yan, M.; Ma, X.; Wang, X. Effect of calcination temperature on the performance of hexaaluminate supported CeO_2 for chemical looping dry reforming. *Fuel Process. Technol.* **2021**, *218*, 106873. [CrossRef]
114. Zheng, Y.; Wei, Y.; Li, K.; Zhu, X.; Wang, H.; Wang, Y. Chemical-looping steam methane reforming over macroporous CeO_2–ZrO_2 solid solution: Effect of calcination temperature. *Int. J. Hydrogen Energy* **2014**, *39*, 13361–13368. [CrossRef]
115. Rydén, M.; Leion, H.; Mattisson, T.; Lyngfelt, A. Combined oxides as oxygen-carrier material for chemical-looping with oxygen uncoupling. *Appl. Energy* **2014**, *113*, 1924–1932. [CrossRef]
116. Long, Y.; Yang, K.; Gu, Z.; Lin, S.; Li, D.; Zhu, X.; Wang, H.; Li, K. Hydrogen generation from water splitting over polyfunctional perovskite oxygen carriers by using coke oven gas as reducing agent. *Appl. Catal. B* **2022**, *301*, 120778. [CrossRef]
117. Lee, M.; Lim, H.S.; Kim, Y.; Lee, J.W. Enhancement of highly-concentrated hydrogen productivity in chemical looping steam methane reforming using Fe-substituted $LaCoO_3$. *Energy Convers. Manag.* **2020**, *207*, 112507. [CrossRef]
118. Zhang, X.; Su, Y.; Pei, C.; Zhao, Z.-J.; Liu, R.; Gong, J. Chemical looping steam reforming of methane over Ce-doped perovskites. *Chem. Eng. Sci.* **2020**, *223*, 115707. [CrossRef]
119. Zhang, X.; Pei, C.; Chang, X.; Chen, S.; Liu, R.; Zhao, Z.J.; Mu, R.; Gong, J. FeO_6 Octahedral Distortion Activates Lattice Oxygen in Perovskite Ferrite for Methane Partial Oxidation Coupled with CO_2 Splitting. *J. Am. Chem. Soc.* **2020**, *142*, 11540–11549. [CrossRef] [PubMed]
120. Xia, X.; Chang, W.; Cheng, S.; Huang, C.; Hu, Y.; Xu, W.; Zhang, L.; Jiang, B.; Sun, Z.; Zhu, Y.; et al. Oxygen Activity Tuning via FeO_6 Octahedral Tilting in Perovskite Ferrites for Chemical Looping Dry Reforming of Methane. *ACS Catal.* **2022**, *12*, 7326–7335. [CrossRef]
121. Huang, C.; Wu, J.; Chen, Y.-T.; Tian, M.; Rykov, A.I.; Hou, B.; Lin, J.; Chang, C.-R.; Pan, X.; Wang, J.; et al. In situ encapsulation of iron(0) for solar thermochemical syngas production over iron-based perovskite material. *Commun. Chem.* **2018**, *1*, 55. [CrossRef]
122. Wang, Y.; Zheng, Y.; Wang, Y.; Wang, H.; Zhu, X.; Wei, Y.; Wang, Y.; Jiang, L.; Yang, Z.; Li, K. Evaluation of Fe substitution in perovskite $LaMnO_3$ for the production of high purity syngas and hydrogen. *J. Power Sources* **2020**, *449*, 227505. [CrossRef]
123. Yin, X.; Wang, S.; Wang, B.; Shen, L. Perovskite-type $LaMn_{1-x}B_xO_{3+\delta}$ (B = Fe, CO and Ni) as oxygen carriers for chemical looping steam methane reforming. *Chem. Eng. J.* **2021**, *422*, 128751. [CrossRef]
124. Shafiefarhood, A.; Galinsky, N.; Huang, Y.; Chen, Y.; Li, F. Fe_2O_3@$La_xSr_{1-x}FeO_3$ Core-Shell Redox Catalyst for Methane Partial Oxidation. *ChemCatChem* **2014**, *6*, 790–799. [CrossRef]
125. Zhao, K.; Chen, J.; Li, H.; Zheng, A.; Huang, Z.; Wei, G.; Zhao, Z.; Wang, X. Investigation of the relationship between electronic properties and reactivity of 3DOM $LaFe_{1-x}Co_xO_3$ for methane reforming to produce syngas. *Int. J. Energy Res.* **2019**, *43*, 7120–7134. [CrossRef]
126. Zhao, K.; Zheng, A.; Li, H.; He, F.; Huang, Z.; Wei, G.; Shen, Y.; Zhao, Z. Exploration of the mechanism of chemical looping steam methane reforming using double perovskite-type oxides $La_{1.6}Sr_{0.4}FeCoO_6$. *Appl. Catal. B* **2017**, *219*, 672–682. [CrossRef]
127. Wang, S.; Guan, B.Y.; Lou, X.W.D. Construction of $ZnIn_2S_4$-In_2O_3 Hierarchical Tubular Heterostructures for Efficient CO_2 Photoreduction. *J. Am. Chem. Soc.* **2018**, *140*, 5037–5040. [CrossRef] [PubMed]
128. Bahmanpour, A.M.; Héroguel, F.; Kılıç, M.; Baranowski, C.J.; Artiglia, L.; Röthlisberger, U.; Luterbacher, J.S.; Kröcher, O. Cu–Al Spinel as a Highly Active and Stable Catalyst for the Reverse Water Gas Shift Reaction. *ACS Catal.* **2019**, *9*, 6243–6251. [CrossRef]
129. Zeng, L.; He, F.; Li, F.; Fan, L.-S. Coal-Direct Chemical Looping Gasification for Hydrogen Production: Reactor Modeling and Process Simulation. *Energy Fuels* **2012**, *26*, 3680–3690. [CrossRef]
130. Bohn, C.D.; Cleeton, J.P.; Müller, C.R.; Chuang, S.Y.; Scott, S.A.; Dennis, J.S. Stabilizing Iron Oxide Used in Cycles of Reduction and Oxidation for Hydrogen Production. *Energy Fuels* **2010**, *24*, 4025–4033. [CrossRef]
131. Liu, W.; Dennis, J.S.; Scott, S.A. The Effect of Addition of ZrO_2 to Fe_2O_3 for Hydrogen Production by Chemical Looping. *Ind. Eng. Chem. Res.* **2012**, *51*, 16597–16609. [CrossRef]
132. Kierzkowska, A.M.; Bohn, C.D.; Scott, S.A.; Cleeton, J.P.; Dennis, J.S.; Müller, C.R. Development of Iron Oxide Carriers for Chemical Looping Combustion Using Sol–Gel. *Ind. Eng. Chem. Res.* **2010**, *49*, 5383–5391. [CrossRef]
133. Chen, S.; Shi, Q.; Xue, Z.; Sun, X.; Xiang, W. Experimental investigation of chemical-looping hydrogen generation using Al_2O_3 or TiO_2-supported iron oxides in a batch fluidized bed. *Int. J. Hydrogen Energy* **2011**, *36*, 8915–8926. [CrossRef]
134. Hafizi, A.; Rahimpour, M. Inhibiting Fe–Al Spinel Formation on a Narrowed Mesopore-Sized $MgAl_2O_4$ Support as a Novel Catalyst for H_2 Production in Chemical Looping Technology. *Catalysts* **2018**, *8*, 27. [CrossRef]
135. Ma, S.; Chen, S.; Soomro, A.; Xiang, W. Effects of supports on hydrogen production and carbon deposition of Fe-based oxygen carriers in chemical looping hydrogen generation. *Int. J. Hydrogen Energy* **2017**, *42*, 11006–11016. [CrossRef]
136. Yüzbasi, N.S.; Armutlulu, A.; Huthwelker, T.; Abdala, P.M.; Müller, C.R. Na-β-Al_2O_3 stabilized Fe_2O_3 oxygen carriers for chemical looping water splitting: Correlating structure with redox stability. *J. Mater. Chem. A* **2022**, *10*, 10692–10700. [CrossRef] [PubMed]
137. Ma, S.; Chen, S.; Soomro, A.; Xiang, W. Effects of CeO_2, ZrO_2, and Al_2O_3 Supports on Iron Oxygen Carrier for Chemical Looping Hydrogen Generation. *Energy Fuels* **2017**, *31*, 8001–8013. [CrossRef]

138. Ma, S.; Chen, S.; Zhao, Z.; Soomro, A.; Zhu, M.; Hu, J.; Wu, M.; Xiang, W. Enhanced Hydrogen Generation for Fe_2O_3/CeO_2 Oxygen Carrier via Rare-Earth (Y, Sm, and La) Doping in Chemical Looping Process. *Energy Fuels* **2018**, *32*, 11362–11374. [CrossRef]
139. Ma, S.; Chen, S.; Ge, H.; Song, T.; Lu, P.; Xiang, W. Synergistic Effects of the Zr and Sm Co-doped Fe_2O_3/CeO_2 Oxygen Carrier for Chemical Looping Hydrogen Generation. *Energy Fuels* **2020**, *34*, 10256–10267. [CrossRef]
140. Do, J.Y.; Son, N.; Park, N.-K.; Kwak, B.S.; Baek, J.-I.; Ryu, H.-J.; Kang, M. Reliable oxygen transfer in $MgAl_2O_4$ spinel through the reversible formation of oxygen vacancies by Cu^{2+}/Fe^{3+} anchoring. *Appl. Energy* **2018**, *219*, 138–150. [CrossRef]
141. Liu, F.; Wu, F.; Liu, J.; Li, Y.; Yang, Y. Experimental and theoretical insights into the mechanism of spinel $CoFe_2O_4$ reduction in CO chemical looping combustion. *Fuel* **2021**, *293*, 120473. [CrossRef]
142. Huang, Z.; Deng, Z.; Chen, D.; Wei, G.; He, F.; Zhao, K.; Zheng, A.; Zhao, Z.; Li, H. Exploration of Reaction Mechanisms on Hydrogen Production through Chemical Looping Steam Reforming Using $NiFe_2O_4$ Oxygen Carrier. *ACS Sustain. Chem. Eng.* **2019**, *7*, 11621–11632. [CrossRef]
143. Kim, Y.; Lim, H.S.; Lee, M.; Kim, M.; Kang, D.; Lee, J.W. Enhanced Morphological Preservation and Redox Activity in Al-Incorporated $NiFe_2O_4$ for Chemical Looping Hydrogen Production. *ACS Sustain. Chem. Eng.* **2021**, *9*, 14800–14810. [CrossRef]
144. Cui, D.; Li, M.; Qiu, Y.; Ma, L.; Zeng, D.; Xiao, R. Improved hydrogen production with 100% fuel conversion through the redox cycle of $ZnFeAlO_x$ oxygen carrier in chemical looping scheme. *Chem. Eng. J.* **2020**, *400*, 125769. [CrossRef]
145. Li, M.; Du, Y.; Qiu, Y.; Ma, L.; Cui, D.; Zhang, S.; Tippayawong, N.; Zeng, D.; Xiao, R. The use of ferrites as highly active oxygen storage materials for chemical looping hydrogen production under intermediate temperature. *Int. J. Hydrogen Energy* **2019**, *44*, 28638–28648. [CrossRef]
146. Zeng, D.; Qiu, Y.; Li, M.; Cui, D.; Ma, L.; Lv, Y.; Zhang, S.; Xiao, R. Ternary Mixed Spinel Oxides as Oxygen Carriers for Chemical Looping Hydrogen Production Operating at 550 °C. *ACS Appl. Mater. Interfaces* **2019**, *11*, 44223–44232. [CrossRef]
147. Hirabayashi, D.; Yoshikawa, T.; Mochizuki, K.; Suzuki, K.; Sakai, Y. Formation of brownmillerite type calcium ferrite ($Ca_2Fe_2O_5$) and catalytic properties in propylene combustion. *Catal. Lett.* **2006**, *110*, 155–160. [CrossRef]
148. Shah, V.; Mohapatra, P.; Fan, L.-S. Thermodynamic and Process Analyses of Syngas Production Using Chemical Looping Reforming Assisted by Flexible Dicalcium Ferrite-Based Oxygen Carrier Regeneration. *Energy Fuels* **2020**, *34*, 6490–6500. [CrossRef]
149. Ismail, M.; Liu, W.; Chan, M.S.C.; Dunstan, M.T.; Scott, S.A. Synthesis, Application, and Carbonation Behavior of $Ca_2Fe_2O_5$ for Chemical Looping H_2 Production. *Energy Fuels* **2016**, *30*, 6220–6232. [CrossRef]
150. Chan, M.S.C.; Liu, W.; Ismail, M.; Yang, Y.; Scott, S.A.; Dennis, J.S. Improving hydrogen yields, and hydrogen:steam ratio in the chemical looping production of hydrogen using $Ca_2Fe_2O_5$. *Chem. Eng. J.* **2016**, *296*, 406–411. [CrossRef]
151. Sun, Z.; Chen, S.; Hu, J.; Chen, A.; Rony, A.H.; Russell, C.K.; Xiang, W.; Fan, M.; Darby Dyar, M.; Dklute, E.C. $Ca_2Fe_2O_5$: A promising oxygen carrier for CO/CH_4 conversion and almost-pure H_2 production with inherent CO_2 capture over a two-step chemical looping hydrogen generation process. *Appl. Energy* **2018**, *211*, 431–442. [CrossRef]
152. Feng, Y.; Wang, N.; Guo, X.; Zhang, S. Reaction mechanism of $Ca_2Fe_2O_5$ oxygen carrier with CO in chemical looping hydrogen production. *Appl. Surf. Sci.* **2020**, *534*, 147583. [CrossRef]
153. You, S.; Ok, Y.S.; Chen, S.S.; Tsang, D.C.W.; Kwon, E.E.; Lee, J.; Wang, C.H. A critical review on sustainable biochar system through gasification: Energy and environmental applications. *Bioresour. Technol.* **2017**, *246*, 242–253. [CrossRef] [PubMed]
154. Hu, Z.; Miao, Z.; Chen, H.; Wu, J.; Wu, W.; Ren, Y.; Jiang, E. Chemical looping gasification of biochar to produce hydrogen-rich syngas using Fe/Ca-based oxygen carrier prepared by coprecipitation. *J. Energy Inst.* **2021**, *94*, 157–166. [CrossRef]
155. Bracciale, M.P.; Damizia, M.; De Filippis, P.; de Caprariis, B. Clean Syngas and Hydrogen Co-Production by Gasification and Chemical Looping Hydrogen Process Using MgO-Doped Fe_2O_3 as Redox Material. *Catalysts* **2022**, *12*, 1273. [CrossRef]
156. Li, F.; Kim, H.R.; Sridhar, D.; Wang, F.; Zeng, L.; Chen, J.; Fan, L.S. Syngas Chemical Looping Gasification Process: Oxygen Carrier Particle Selection and Performance. *Energy Fuels* **2009**, *23*, 4182–4189. [CrossRef]
157. Li, F.; Zeng, L.; Velazquez-Vargas, L.G.; Yoscovits, Z.; Fan, L.-S. Syngas chemical looping gasification process: Bench-scale studies and reactor simulations. *AlChE J.* **2010**, *56*, 2186–2199. [CrossRef]
158. Luo, C.; Dou, B.; Zhang, H.; Liu, D.; Zhao, L.; Chen, H.; Xu, Y. Co-production of hydrogen and syngas from chemical looping water splitting coupled with decomposition of glycerol using Fe-Ce-Ni based oxygen carriers. *Energy Convers. Manag.* **2021**, *238*, 114166. [CrossRef]
159. Sun, S.; Zhao, M.; Cai, L.; Zhang, S.; Zeng, D.; Xiao, R. Performance of CeO_2-Modified Iron-Based Oxygen Carrier in the Chemical Looping Hydrogen Generation Process. *Energy Fuels* **2015**, *29*, 7612–7621. [CrossRef]
160. Aston, V.J.; Evanko, B.W.; Weimer, A.W. Investigation of novel mixed metal ferrites for pure H_2 and CO_2 production using chemical looping. *Int. J. Hydrogen Energy* **2013**, *38*, 9085–9096. [CrossRef]
161. Liu, S.; He, F.; Huang, Z.; Zheng, A.; Feng, Y.; Shen, Y.; Li, H.; Wu, H.; Glarborg, P. Screening of $NiFe_2O_4$ Nanoparticles as Oxygen Carrier in Chemical Looping Hydrogen Production. *Energy Fuels* **2016**, *30*, 4251–4262. [CrossRef]
162. Scheffe, J.R.; Allendorf, M.D.; Coker, E.N.; Jacobs, B.W.; McDaniel, A.H.; Weimer, A.W. Hydrogen Production via Chemical Looping Redox Cycles Using Atomic Layer Deposition-Synthesized Iron Oxide and Cobalt Ferrites. *Chem. Mater.* **2011**, *23*, 2030–2038. [CrossRef]
163. Xu, C.; Zhang, Y.; Chen, J.; Lin, J.; Zhang, X.; Wang, Z.; Zhou, J. Enhanced mechanism of the photo-thermochemical cycle based on effective Fe-doping TiO_2 films and DFT calculations. *Appl. Catal. B* **2017**, *204*, 324–334. [CrossRef]

164. Docao, S.; Koirala, A.R.; Kim, M.G.; Hwang, I.C.; Song, M.K.; Yoon, K.B. Solar photochemical–thermal water splitting at 140 °C with Cu-loaded TiO_2. *Energy Environ. Sci.* **2017**, *10*, 628–640. [CrossRef]
165. Wu, Q.; Li, Z.; Zhang, X.; Huang, W.; Ni, M.; Cen, K.; Zhang, Y. Enhanced defect-water hydrogen evolution method for efficient solar utilization: Photo-thermal chemical coupling on oxygen vacancy. *Chem. Eng. J.* **2021**, *408*, 127248. [CrossRef]
166. Wu, Q.; Li, Z.; Zhang, X.; Xu, C.; Ni, M.; Cen, K.; Zhang, Y. Oxygen-vacancy-anchoring NiO loading towards efficient hydrogen evolution via photo-thermal coupling reaction. *J. Energy Chem.* **2021**, *61*, 77–87. [CrossRef]
167. Zeng, D.; Qiu, Y.; Zhang, S.; Ma, L.; Li, M.; Cui, D.; Zeng, J.; Xiao, R. Synergistic effects of binary oxygen carriers during chemical looping hydrogen production. *Int. J. Hydrogen Energy* **2019**, *44*, 21290–21302. [CrossRef]